Encoding of inflammatory hyperalgesia in mice spinal cord

Omer Barkai[1,2], Rachely Butterman[1,2], Ben Katz[1,2], Shaya Lev[1,2]

and Alexander M Binshtok[1,2*]

[1]Department of Medical Neurobiology; Institute for Medical Research Israel-Canada, The Hebrew University-Hadassah School of Medicine, Jerusalem, Israel, 91120;

[2]The Edmond and Lily Safra Center for Brain Sciences, The Hebrew University of Jerusalem, Israel

**Correspondence:* alexander.binshtok@mail.huji.ac.il

Summary

Inflammation modifies the input-output properties of peripheral nociceptive neurons, thus leading to hyperalgesia, i.e., changes in the perception of noxious heat stimuli such that the same stimulus produces enhanced pain. The increased nociceptive output enters the superficial dorsal spinal cord (SDH), which comprises the first CNS network integrating the noxious information. Here we used *in vivo* calcium imaging and a computational approach to investigate how the SDH network in mice encodes the injury-mediated abnormal input from peripheral nociceptive neurons. We show the application of noxious heat stimuli to the mice hind paw in naïve conditions before induction of injury affects the activity of 70% of recorded neurons by either increasing or suppressing it. Application of the same noxious heat stimuli to hyperalgesic skin leads to activation of previously non-responded cells and de-suppression of the "suppressed" neurons. We demonstrate that reduction in synaptic inhibition mimics the response to the noxious stimuli in the hyperalgesic conditions. Using a computational model of SDH network, we predict that inflammation-induced "disinhibition"-like changes result in increased activity of excitatory projection neurons. Our model also predicts that the observed "disinhibitory" effect of hyperalgesic stimuli does not require changes in the inhibitory transmission and may result from the SDH networks' intrinsic cytoarchitecture.

Keywords: nociception, hyperalgesia, inflammatory pain, superficial dorsal spinal cord, hyperexcitability, noxious heat

Introduction

Noxious information is detected by primary afferent nociceptive neurons and transmitted to the superficial laminae of the dorsal spinal cord (SDH). There, the information undergoes through a complex neuronal network, composed of excitatory and inhibitory interneurons. The output from this network is transmitted via projection neurons to higher brain centers, thus sculpturing the sensation and perception of pain. Tissue inflammation leads to changes in the activity patterns of peripheral nociceptive neurons (Barkai et al., 2017, 2019; Goldstein et al., 2019; Yarmolinsky et al., 2016), thus modifying the input and output of the superficial spinal dorsal horn (Laminae I-II, SDH) nociceptive network (Barkai et al., 2020; Cho et al., 2016). While the mechanisms underlying inflammatory-mediated hyperexcitability of nociceptive neurons have been described (see for example (Basbaum et al., 2009; Binshtok et al., 2008; Gudes et al., 2015; Hucho and Levine, 2007), how the SDH neuronal network accommodates abnormal input from hyperexcitable nociceptors and how these enhanced inputs, affect the SDH network's output towards higher brain centers, leading to inflammatory pain, is not well understood.

Traditionally, noxious heat stimuli-responsive spinal neurons have been investigated by *ex vivo* preparations or *in vivo* electrophysiology. These studies reveal molecular, intrinsic and functional diversity of dorsal horn neurons (Braz et al., 2014; Duan et al., 2014; Foster et al., 2015; Hughes et al., 2020; Todd, 2010; Wang et al., 2013). Changes in the synaptic connectivity following inflammation or nerve injury have also been detailed (Balasubramanyan et al., 2006; Schoffnegger et al., 2006; Zhang et al., 2018). However, studies describing the response of spinal cord neurons to noxious heat stimuli applied to target organs *in vivo* have been limited due to technical constraints. Patch-clamp electrophysiology allows the recording of single-cell activity, whereas local field potential recordings enable measuring potential changes of neuronal populations but in limited areas. Recently, several studies have shown ways to overcome these technical limitations by applying *in vivo* two-photon imaging (2PLSM) from the spinal cord in anesthetized animals (Harding et al., 2020; Johannssen and Helmchen, 2010, 2013; Ran and Chen, 2019). These *in vivo* dorsal horn imaging preparations allow simultaneous optical recording of the activity of multiple (~200) neurons with a single-cell resolution during noxious stimulation of the skin (Johannssen and Helmchen, 2010, 2013; Kohro et al., 2020; Ran et al., 2016). This approach allowed for the first time to detail how the SDH network codes thermal stimuli, showing that the heat applied to the skin is represented in a gradual manner, such that application of noxious (above 42°C) stimulus to the skin activates distinct populations of neurons (Ran et al., 2016). These results unravel how stimuli are

represented by SDH neurons in normal conditions. However, network analysis in pathological conditions, such as hyperalgesia, i.e., enhanced sensitivity to noxious heat stimuli following injury-induced inflammation, is still missing. Here we asked how the stimuli representation in the SDH network changes in inflammatory conditions to produce an altered, hyperalgesic perception of thermal stimuli after injury.

To address this question, we studied the SDH network for coding changes in thermo-sensation by examining the consequences of heat-induced inflammation, a physiological and clinical insult that rapidly induces changes in thermal perception (Coderre and Melzack, 1985; Shields et al., 2012). We developed a mouse model of a burn injury which induces inflammation and thermal hyperalgesia and could be used together with the measurement of cell activity. We utilized this model to visualize the representation of noxious heat by the SDH neuronal ensemble before the injury and detail how this representation changes after injury. We show that in normal conditions, about 40% of the recorded SDH neurons increase their activity following application of the noxious heat stimulus to the mice hind paw skin ("activated" neurons), about 30% of the neurons suppress their activity ("suppressed" neurons), and another 30% are non-responsive during the noxious heat stimulus ("non-responsive" neurons). Application of the noxious heat stimulus to hyperalgesic skin, following tissue injury, leads to an overall increase of the SHD network activity via disinhibition-like changes, by reducing in suppression (de-suppression) of the "suppressed" neurons and unmasking the activity of "non-responsive" neurons. We show that the blockade of inhibitory transmission in SDH mimics the SDH activity patterns evoked by the noxious heat stimuli applied to the hyperalgesic skin. By implementing a computational model of the SDH network, which we built, we demonstrate that the intrinsic SDH network's cytoarchitecture is by itself prone to disinhibition even without modulating inhibitory synaptic transmission. Our model predicts that increased input in modeled inflammatory conditions leads to a substantial increase in excitatory neuronal firing, thus increasing the SDH network output towards higher brain centers. Our results demonstrate how pain-related spinal cord circuitry represents input from the periphery and how this representation changes in pathological conditions underlying the development of inflammatory hyperalgesia.

Results

We examined how superficial spinal dorsal horn (Laminae I-II, SDH) neurons generate a network representation of enhanced input from the peripheral thermosensitive nociceptive neurons, thus encoding inflammation-induced thermal hyperalgesia. We hypothesized that increased input from the periphery would increase the overall responsiveness of SDH neurons. If it is true, would this increase be achieved by enhanced responsiveness of the neurons that responded to noxious heat before the inflammation? Or increased input from the hyperexcitable peripheral neurons would modify the network response signature to noxious heat? To answer these questions, we performed *in vivo* two-photon (2PLSM) imaging to record noxious (~ 49°C) thermal stimuli-evoked calcium signals in a large (~200 neurons/mice) population of Laminae I-II SDH neurons in anesthetized mice before and after local burn injury (**Figure 1A**). We stimulated the glabrous skin of the right hind paw with a custom-made Peltier device which was held at a baseline temperature of 32°C (Paricio-Montesinos et al., 2020; Ran et al., 2016; Yarmolinsky et al., 2016). We then applied noxious thermal stimuli by elevating the temperature at a fast rate (~2.5°C/s) to ~49°C and holding this temperature for 20 s. During this stimulation, we recorded changes in intracellular Ca^{2+} from Oregon Green 488 Bapta-1 AM (OGB)-labeled Laminae I-II SDH cells (**Figure 1A**, *Before*). To examine the changes in SDH neuronal activity following local inflammation, we induced a mild burn injury by applying an intensive thermal stimulus of 50 to 65°C for ~45 s, at the same hind paw using the same stimulation source used for noxious heat application (**Figure 1A**, *below*). A second noxious thermal stimulus of ~49°C was applied, 1 hour after generating the injury, to examine changes in SDH network representation of the inflammatory hyperalgesic state (**Figure 1A**, After). To minimize time-dependent drift in the field of view and photo-bleaching, we allowed only 1 hour for the development of inflammation. To assure that the injury protocol and one-hour time window are sufficient to induce tissue injury and inflammatory hyperalgesia, we examined the inflammation signs and pain-related behaviors following the same stimulation paradigm in separate groups of animals. Stimulation of the hind paw with the same "intensive, injury-inducing" stimulus, used in the two-photon apparatus under the same conditions (*see Methods*), produced substantial redness of the glabrous skin and a significant increase in the paw width (**Figure 1B**). Notably, application of the "injury-inducing" stimulus led to a significant decrease in paw withdrawal latency following stimulation with radiant heat, one hour after injury (**Figure 1C**) and a significant reduction of the active exploration distance at the near-noxious heat threshold (41°C) open field test (**Supplementary Figure 1A**). Altogether, these results suggest that application of "intensive, injury-inducing" stimulus induces local

inflammation accompanied by thermal hyperalgesia, we therefore hereafter referred to this stimulus as "hyperalgesia-inducing stimulus."

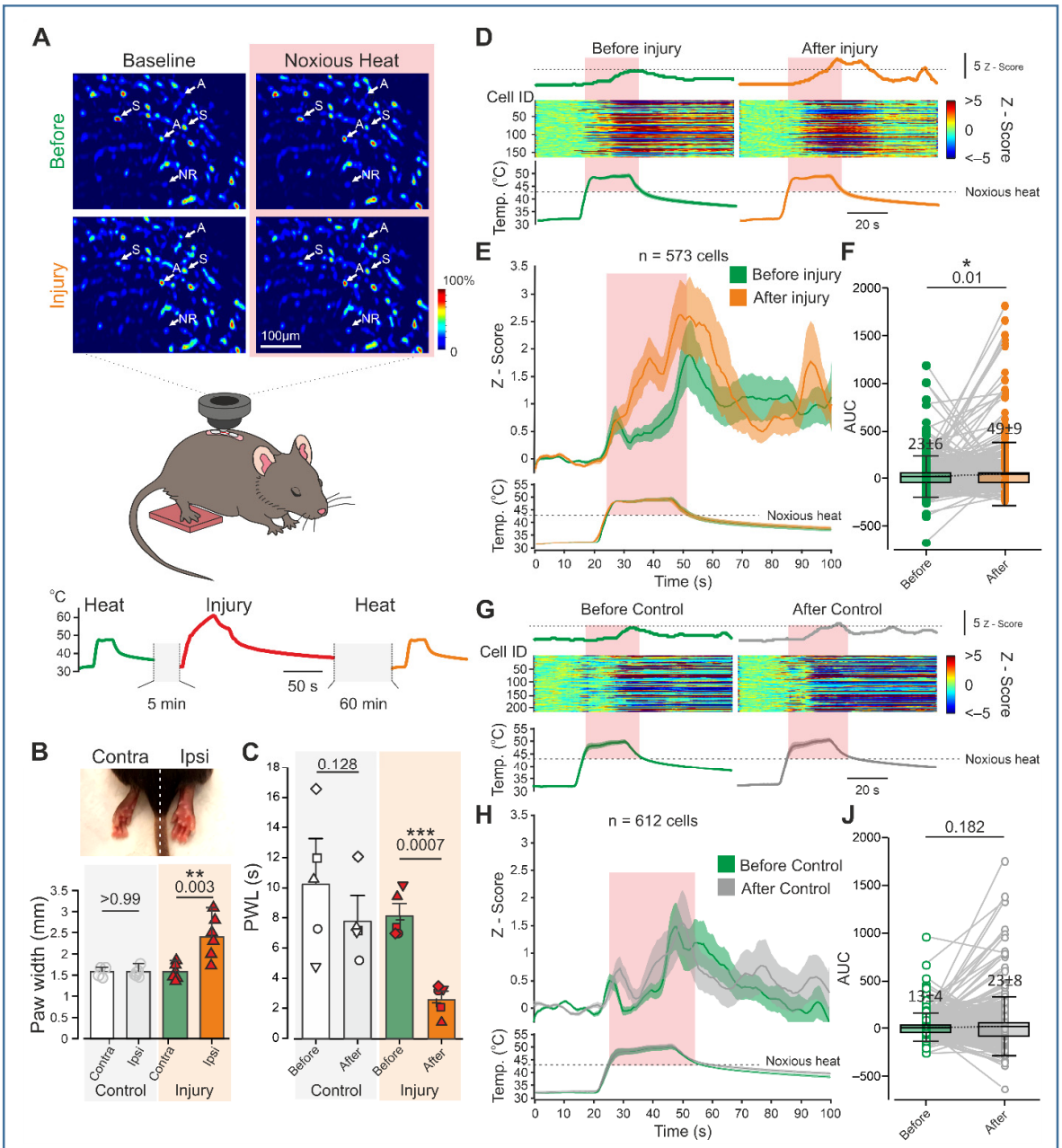

Figure 1. Thermal hyperalgesia is accompanied by increased activation of the superficial spinal dorsal horn (SDH) neurons. A. Scheme depicting the experimental procedure. *In vivo* recordings of changes in intracellular Ca^{2+} (measured as changes in OGB fluorescence) in cells composing the right Laminae I-II of the spinal dorsal horn (SDH) at vertebra level T12 (~ level of L5 segment). Experiments were performed in anesthetized mice using 2PLSM. The changes in intracellular Ca^{2+} were evoked by noxious heat stimulation (showed in the lower panel) of the right hind paw using a custom Peltier device. In control group, two similar noxious

stimulations were applied 1 hour apart (*before and after control).* In the "injury" group, 5 minutes after the first noxious stimulation, burn injury was induced by applying hyperalgesia-inducing stimulus to the right hind paw (*lower panel*). One hour after the induction of the burn injury, a second noxious heat stimulus was applied (*lower panel*). *Inset*, pseudocolor photomicrographs of SDH cells before application of the first noxious heat stimulus (*Baseline, Before*), after application of the first noxious heat stimulus (*Before, Noxious Heat*), and before (*Injury, Baseline*) and after application of the second noxious heat stimulus (*Injury, Noxious Heat*) after the burn injury. Arrows outline different response patterns of SDH cells: A - cells that were activated following first noxious heat stimulus ("activated"); S – cells whose activity was suppressed following first noxious heat stimulus ("suppressed") and NR – cell which did not respond to the noxious heat stimulus ("non-responsive"). **B.** *Upper*, an image of the hind paws contra- and ipsilateral to application of the hyperalgesia-inducing stimulus used in *A* for inducing the burn injury. Note the redness and the edema of the injured hind paw. *Lower*, bar graph and individual values depicting the paw thickness before and after application of the hyperalgesia-inducing stimulus to the right hind paw (*injury*) compared to control group, which underwent the same procedure but without activating the Peltier device. n = 6 mice in each group, unpaired *t*-test. **C.** Box plots and paired individual values of paw withdrawal latencies (PWL) measured following focal application of radiant heat before and after application of hyperalgesia-inducing stimulus (*Injury*) or in control conditions (*Control*). Paired *t*-test, n=5 mice in the "control" group and n = 6 mice in the "injury" group. **D.** *Middle*, representative activity heat maps for 166 cells in the same field of view (FOV) during application of noxious heat stimulus to the paw before and after induction of hyperalgesia-mediating injury. The averaged (means) changes in activity are shown above the heat maps. The dotted line is aligned to the peak of the mean response before the injury. The stimuli are shown below the heat maps. The noxious (above 42°C) component of the stimulus is outlined by the pink shadow. Representative of 4 mice. **E.** Changes in intracellular Ca^{2+} following application of the noxious heat stimulus (depicted below) before (*green*) and 1 hour after (*orange*) induction of the burn injury (Z-Score; mean ± SEM) from all recorded cells in 4 mice. The noxious (above 42°C) component of the stimulus is outlined by the pink shadow. n=573 cells from 4 mice. Note increase in the cell activity following the application of the noxious heat stimulus to the injured paw. **F.** Box plots and paired individual values of changes in AUC (arbitrary units, AU) of the response (shown in *E*, Z-score), before (*green*) and 1 hour after (*orange*) induction of the injury. Paired *t*-test, n=573 cells from 4 mice. **G.** Same as in *D*, but showing the representative activity heat maps for 209 cells in the same field of view (FOV) in control conditions, i.e., following

application of first and second noxious heat stimuli, 1 hour apart without applying the hyperalgesia-inducing stimulus. Note that the response to the first noxious heat stimulus is similar to that of the second noxious heat stimulus. Representative of 4 mice. **H.** Same as in *E*, but showing changes in intracellular Ca^{2+} of all recorded cells in 4 mice in control condition, i.e., following application of first (*green*) and second noxious heat stimuli (*grey*), 1 hour apart without applying the hyperalgesia-inducing stimulus. Note that the response to the first noxious heat stimulus is similar to that of the second noxious heat stimulus, suggesting the stability of the response. n=612 cells from 4 mice. **J.** Same as in *F*, but comparing AUC of the responses to the noxious heat in control conditions. Paired *t*-test, n=612 cells from 4 mice. The data points shown in *F* and *J* were collected and analyzed over the time of the noxious part of stimulus (*see Methods*). Box plots depict the mean and 25 and 75 percentiles, and the whiskers depict SD. Numbers above the boxes are means ± SEM. For comparison of changes in the mean amplitude of the responses, see **Supplementary Figure 1**.

Consequently, we utilized the hyperalgesia-inducing stimulus to study the changes in the response of the SDH network to the noxious heat stimulus applied to hyperalgesic skin and compare them to SDH responses in the control conditions, in which the second noxious heat stimulus was applied one hour after the first noxious heat stimulus but without preceding injury. We show that the application of the noxious heat stimulus produced an overall increase in neuronal activity (**Figure 1D, G** *before*, **1E, H,** *green*). This evoked activity pattern was stereotypical as the application of the second noxious heat stimulus to control animals, which did not undergo tissue injury, 1 hour after the application of the first noxious heat stimulus, led to a similar response (**Figure 1G**, *after*, **H, J,** *grey*, **Supplementary Figure 1B**, *right*). Notably, SDH astrocytes, which were shown to respond to the application of capsaicin (Kohro et al., 2020) and electrical stimulation (Cirillo et al., 2012) also responded to application of the noxious heat stimuli (**Supplementary Figure 2A**, *red*).

Application of noxious heat stimulus 1 hour after hyperalgesia-inducing stimulus led to an overall increase in neuronal activity (**Figure 1D**, *after,* **1E,** *orange*), demonstrated by a significant overall increase in the response area under the curve (AUC, **Figure 1F**), and mean amplitude (**Supplementary Figure 1B**, *left*), measured during the noxious part of stimuli (*see Methods*). The changes observed in SDH cells were attributed to the changes in the neuronal

activity since SDH astrocytes did not show an overall change in activity following the application of the noxious heat stimuli to hyperalgesic skin (**Supplementary Figure 2A-C**).

If indeed the input from the inflamed tissue results in increase of SDH activity, would it be achieved by increasing the responsiveness of the neurons that responded to noxious heat before the inflammation? Or increased input from the hyperexcitable peripheral neurons would modify the network response signature to noxious heat? Importantly we detected that the first noxious heat stimulus led to distinctive responses in SDH neurons (**Figure 1A,** *arrows*). The majority (about 40%) of the cells underwent activation in response to the first noxious heat stimulus, thus we named them "activated" (**Figure 1A***, arrows "A,"* **Figure 4A, D,** *insets*). About 30% of cells labeled by OGB did not respond to the first noxious heat, thus we named them "non-responsive" (**Figure 1A,** *arrow "NR";* **Figure 2A, D,** *insets*). Additionally, a notable subset of cells, about 30%, was suppressed by the application of the first noxious heat stimulus, thus we named them "suppressed" (**Figure 1A,** *arrows "S";* **Figure 2A, D,** *insets*). Noteworthy, the categorization of cell responses into "activated," "suppressed," and "non-responsive" cells do not necessarily overlap with the excitatory and inhibitory nature of the SDH neurons as the first describes the cell response, while the second its output.

The increase of the overall SDH network activity in response to the second noxious heat stimulus could result from the inflammation-mediated recruitment of "non-responsive" cells. To examine this hypothesis, we monitored the activity of "non-responsive" cells following the application of the second noxious heat stimulus on hyperalgesic skin. We show that application of the second noxious heat stimulus in hyperalgesic conditions led to a small but significant overall increase in activity of previously "non-responsive" cells (**Figure 2A, B**; **Supplementary Figure 3A**). This increase was observed only following injury since the application of a second noxious heat stimulus in control conditions did not lead to an overall activation of previously "non-responding" cells (**Figure 2C, D**; **Supplementary Figure 3B**). It is noteworthy that in inflammatory conditions, only 51% of the previously "non-responding" cells changed their activity pattern (**Supplementary Figure 4A**, *inset*) such that 30% became activated (**Supplementary Figure 4A-C**) while 22% of the cells became suppressed (**Supplementary Figure 4D-F**). However, the activation of the "non-responsive" cells was substantially higher than the suppression of the "non-responsive" cells (**Supplementary Figure 4B, C** vs. **Supplementary Figure 4E, F**), possibly explaining the overall increase in the activity of the "non-responsive" cells following hyperexcitable input from the injured skin

(**Figure 2E, F**). The rest of the "non-responsive" cells (48%), did not respond to the noxious heat stimulus applied to the injured skin (**Supplementary Figure 4G-I**).

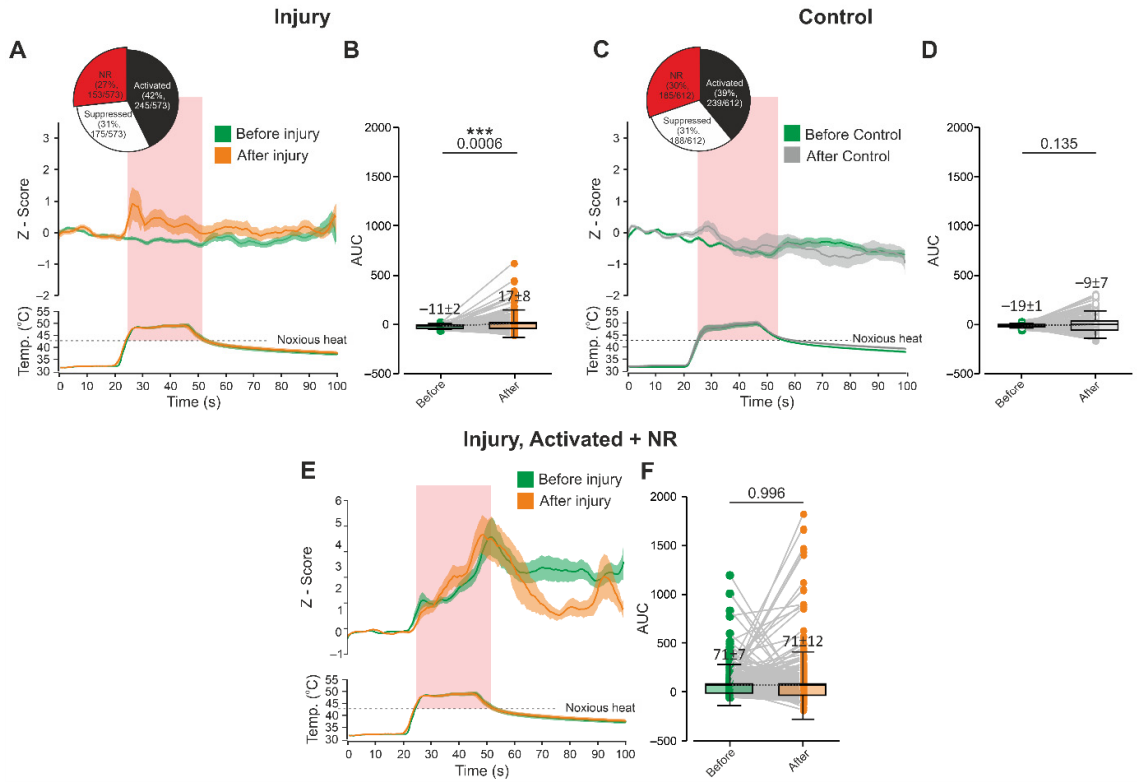

Figure 2. The noxious heat stimuli applied to the hypersensitive skin trigger the activation of the "non-responsive" SDH cells. A. Changes in intracellular Ca^{2+} in all recorded "non-responsive" (NR) cells from 4 mice, following application of the heat stimulus (depicted below) before (*green*) and 1 hour after (*orange*) induction of the burn injury (Z-Score, mean ± SEM). The noxious (above 42°C) component of the stimulus, is outlined by the pink shadow. n=153 cells from 4 mice. Note an increase in the activity following the application of the noxious heat stimulus to the injured paw. *Inset,* pie chart outlining (*red*) the fraction of cells that did not respond to the application of the first noxious heat stimulus ("non-responsive," NR), before the induction of the burn injury, amongst the cells that either increased ("activated") or decreased their activity ("suppressed") their activity following application of the first noxious heat stimulus. **B.** Box plots and paired individual values of changes in the responses' AUC of the "NR" cells before (*green*) and 1 hour after (*orange*) induction of the injury. Paired *t*-test, n=153 cells from 4 mice. **C.** Same as *A*, but showing changes in the activity of all recorded "NR" cells from 4 mice following application of the first (*green*) and second

(*gray*) noxious heat stimuli (depicted below) in control conditions. n=185 cells from 4 mice. *Inset*, same as *A*, but outlining the fraction of "NR" cells amongst "activated" and "suppressed" cells in control conditions (i.e., without applying the hyperalgesia-inducing stimulus). **D.** Box plots and paired individual values of changes in the responses' AUC of the "NR" cells following application of the first (*green, before*) and second (*gray, after*) noxious heat stimuli in control conditions. Paired *t*-test, n=185 cells from 4 mice. **E.** Combined Z-Score (mean ± SEM) of changes in intracellular Ca^{2+}, in the "activated" and "NR" cells, following application of the heat stimulus (depicted below) before (*green*) and 1 hour after (*orange*) induction of the burn injury. The noxious (above 42ºC) component of the stimulus is outlined by the pink shadow. n=398 cells from 4 mice. Note that combining "activated" and "NR" cell activity is not sufficient to produce an inflammation-mediated increase in overall activity. **F.** Box plots and paired individual values of the combined "activated" and "NR" changes in the responses' AUC of the cells before (*green*) and 1 hour after (*orange*) induction of injury. Paired *t*-test, n=398 cells from 4 mice. The data points shown in *B, D,* and *F* were collected and analyzed over the time of the noxious part of stimulus (*see Methods*). Box plots depict the mean and 25 and 75 percentiles, and the whiskers depict SD. Numbers above the boxes are means ± SEM. For comparison of changes in the mean amplitudes of the responses, see **Supplementary Figure 3**.

Would the activation of the previously "non-responsive" cells following injury be sufficient to produce the inflammation-mediated increase in the overall activity of the SDH network? Since we show that inflammation does not induce an increase in the response of the "activated" cells, we examined if the combined effect of the "activated" cells together with the effect of the "non-responsive" cells would lead to a significantly higher response than the response to the first noxious heat stimulus applied before the induction of the injury (**Figure 2E, F; Supplementary Figure 3C**). We show that summation of the activation of the "non-responsive" cells and the activation of the "activated" cells was insufficient to account for the increased response to the second noxious heat stimulus observed in the hyperalgesic conditions (**Figure 2E, F; Supplementary Figure 3C**).

Another option that might explain the overall increase in response to noxious heat stimulus applied in the inflammatory conditions is activity de-suppression in cells that reduced their activity following the application of the first noxious heat stimulus ("suppressed" cells).

Indeed, we show that "suppressed" cells were significantly less suppressed to the second noxious heat stimulus applied to the hyperalgesic skin (**Figure 3A-C**; **Supplementary Figure 5**, *left*). In contrast, application of second noxious heat stimulus in control conditions produced a similar suppression in the activity as following the application of the first stimulus (**Figure 3D-F**; **Supplementary Figure 5**, *right*). Collectively, these data imply that the overall increase in SDH circuit activity following hyperexcitable input from the periphery is partly due to the "disinhibition" of the "suppressed" cells, leading to a decrease in their activity inhibition, and in part by activation of cells which did not respond to the application of the noxious heat stimulus before the injury.

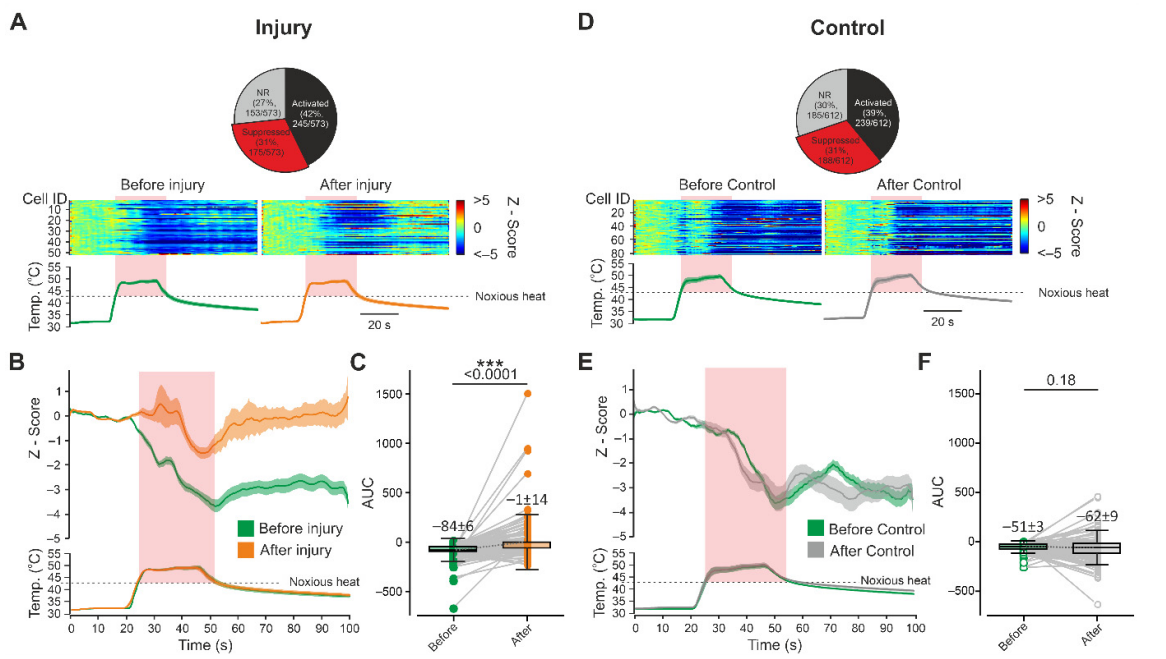

Figure 3. Noxious heat stimuli applied on hyperalgesic skin trigger decrease in activity suppression of the SDH neurons. A. Representative heat maps of the activity of 52 "suppressed" cells in the same field of view (FOV) during application of noxious heat stimulus to the paw before and after induction of hyperalgesia-mediating injury. The stimuli are shown below the heat maps. The noxious (above 42°C) component of the stimulus is outlined by the pink shadow. Representative of 4 mice. *Inset,* pie chart outlining (*red*) the fraction of cells that decreased their activity ("suppressed") following application of the first noxious heat stimulus, before the induction of the burn injury, amongst the cells which either increased their activity ("activated") following application of the first noxious heat stimulus or did not respond to the application of the first noxious heat stimulus ("non-responsive," NR). **B.** Changes in intracellular Ca^{2+} in all recorded "suppressed" cells from 4 mice, following application of the

heat stimulus (depicted below) before (*green*) and 1 hour after (*orange*) induction of the burn injury (Z-score, mean± SEM). The noxious (above 42°C) component of the stimulus is outlined by the pink shadow. n=175 cells from 4 mice. Note a substantial decrease in the activity suppression following application of the noxious heat stimulus to the injured paw. **C.** Box plots and paired individual values of changes in the responses' AUC of the "suppressed" cells before (*green*) and 1 hour after (*orange*) induction of the injury. Paired *t*-test, n=175 cells from 4 mice. **D.** Same as *A*, but showing the representative activity heat maps for 82 "suppressed" cells in the same field of view (FOV) during application of noxious heat stimulus to the paw in control conditions. Representative of 4 mice. *Inset*, same as *A*, but outlining the fraction of "suppressed" cells amongst "activated" and "non-responsive" (NR) cells in control conditions (i.e., without applying the hyperalgesia-inducing stimulus). **E.** Same as *B*, but showing changes in the cell activity following application of the first (*green*) and second (*gray*) noxious heat stimuli (depicted below) in control conditions. n=188 cells from 4 mice. **F.** Box plots and paired individual values of changes in the responses' AUC of the "activated" cells following application of the first (*green, before*) and second (*gray, after*) noxious heat stimuli in control conditions. Paired *t*-test, n=188 cells from 4 mice. The data points shown in *C* and *F* were collected and analyzed over the time of the noxious part of stimulus (*see Methods*). Box plots depict the mean and 25 and 75 percentiles, and the whiskers depict SD. Numbers above the boxes are means ± SEM. For comparison of changes in the responses' mean amplitude, see **Supplementary Figure 5**.

Finally, the increase in response to the second noxious heat stimulus, which was applied to the hyperalgesic skin, could result from increase in the activity of the "activated" neurons. We show that in control conditions, the responses of the "activated" cells were stereotypic since an application of the second noxious heat stimulus did not change their response AUC and amplitude (**Figure 4D-F**; **Supplementary Figure 6**, *right*). Application of the second noxious heat stimulus to the hyperalgesic skin also had no overall effect on the AUC and the mean amplitude of the "activated" cells (**Figure 4A-C**; **Supplementary Figure 3**, *left*). It is noteworthy that in all experiments, we used a relatively low acquisition rate (2 Hz) to minimize fluorescence photo-bleaching. Since a low acquisition rate does not allow recording in high activity time resolution, the resulting calcium signals only allow interpretation of changes relative to a global baseline, before vs. after stimulation, and not to identify changes in spontaneous baseline activity, which may also be affected by the inflammation-induced

nociceptive hyperexcitability (Binshtok et al., 2008; Yarmolinsky et al., 2016). The relatively low sampling frequency we used here does not permit analyzing changes in spontaneous activity of the SDH neurons. Moreover, due to photo-bleaching, we were unable to perform continuous recording during the whole experiment, which takes more than 2 hours. Instead, we recorded only a short baseline followed by a stimuli-induced response in both conditions. Thus, we are unable to normalize the response to the noxious heat stimuli in the inflammatory conditions to the baseline at the beginning of the experiment due to the time-dependent changes in cell position and fluorescence. We, therefore, calculated the amplitude of the response in the inflammatory conditions by normalizing it to the baseline we obtained in these conditions. It is plausible that this baseline is higher as a result of inflammation-mediated increase bombardment of the SDH neurons from the peripheral neurons. Because we measure the increase in the response amplitude relative to the global baseline, the resulting normalized response to the higher baseline may mask the real magnitude of the observed effect, thus underestimating the actual changes in the activity of SHD neurons, primarily of the "activated" neurons.

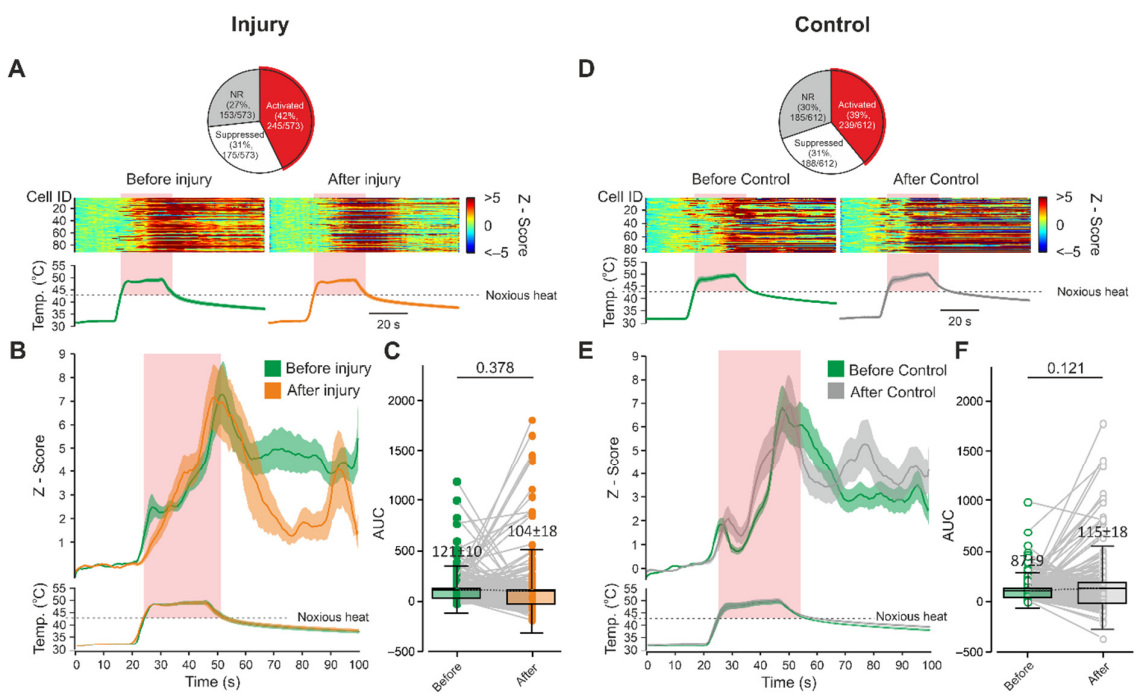

Figure 4. Injury-mediated increase in overall SDH activation does not result from changes in the response of the "activated" cells. A. Representative activity heat maps for 93 "activated" cells in the same field of view (FOV) during application of noxious heat stimulus to the paw before and after induction of hyperalgesia-mediating injury. The stimuli are shown

below the heat maps. The noxious (above 42°C) component of the stimulus is outlined by the pink shadow. Representative of 4 mice. *Inset,* pie chart outlining (*red*) the fraction of cells that increased their activity following the application of the first noxious heat stimulus ("activated"), before the induction of the burn injury, amongst the cells which either decreased their activity ("suppressed") following application of the first noxious heat stimulus or did not respond to the application of the first noxious heat stimulus ("non-responsive," NR). **B.** Changes in intracellular Ca^{2+} in all recorded "activated" cells from 4 mice, following application of the heat stimulus (depicted below) before (*green*) and 1 hour after (*orange*) induction of the burn injury (Z-Score, mean ± SEM). The noxious (above 42°C) component of the stimulus is outlined by the pink shadow. n=245 cells from 4 mice. Note, no change in the neuronal activity following application of the noxious heat stimulus to the injured paw. **C.** Box plots and paired individual values of changes in AUC of the responses (shown in *B,* Z-score) of the "activated" cells before (*green*) and 1 hour after (*orange*) induction of injury. Paired *t*-test, n=245 cells from 4 mice. **D.** Same as *A*, but showing the representative activity heat maps for 85 "activated" cells in the same field of view (FOV) during application of noxious heat stimulus to the paw in control conditions. Representative of 4 mice. *Inset*, same as *A*, but outlining the fraction of "activated" cells amongst "suppressed" and "non-responsive" (NR) cells in control conditions (i.e., without applying the hyperalgesia-inducing stimulus). **E.** Same as *B*, but showing changes in intracellular Ca^{2+} following application of the first (*green*) and second (*gray*) noxious heat stimuli (depicted below) in control conditions. n=239 cells from 4 mice. **F.** Box plots and paired individual values of changes in the responses' AUC (shown in *E*) of the "activated" cells following application of the first (*green, before*) and second (*gray, after*) noxious heat stimuli in control conditions. Paired *t*-test, n=239 cells from 4 mice. The data points shown in *C* and *F* were collected and analyzed over the time of the noxious part of stimulus (*see Methods*). Box plots depict the mean and 25 and 75 percentiles, and the whiskers depict SD. Numbers above the boxes are means ± SEM. For comparison of changes in the mean amplitudes of the responses, see **Supplementary Figure 6**.

To examine the changes in the activity of SDH cells taking into account the increased baseline, we modeled the SDH network utilizing a conductance-based adaptive exponential (CadEx, Górski et al., 2021) integrate-and-fire model (**Figure 5A**). This model allows performing large network simulations with simplified models reproducing neuronal firing properties (Górski et al., 2021). We constructed a biologically constrained model of a superficial spinal dorsal horn

Laminae I-II, composed of 70% excitatory and 30% inhibitory spiking neurons (Polgár et al., 2013; Prescott and Ratté, 2012; Todd, 2010) connected to each other (**Figure 5A, B**). The intrinsic connectivity of the excitatory and inhibitory neurons within the network was unidirectional (Lu and Perl, 2003, 2005), and the synaptic weights of excitatory and inhibitory synapses connected to excitatory neurons was higher than that connected to inhibitory neurons (Lee et al., 2019, *see Methods*).

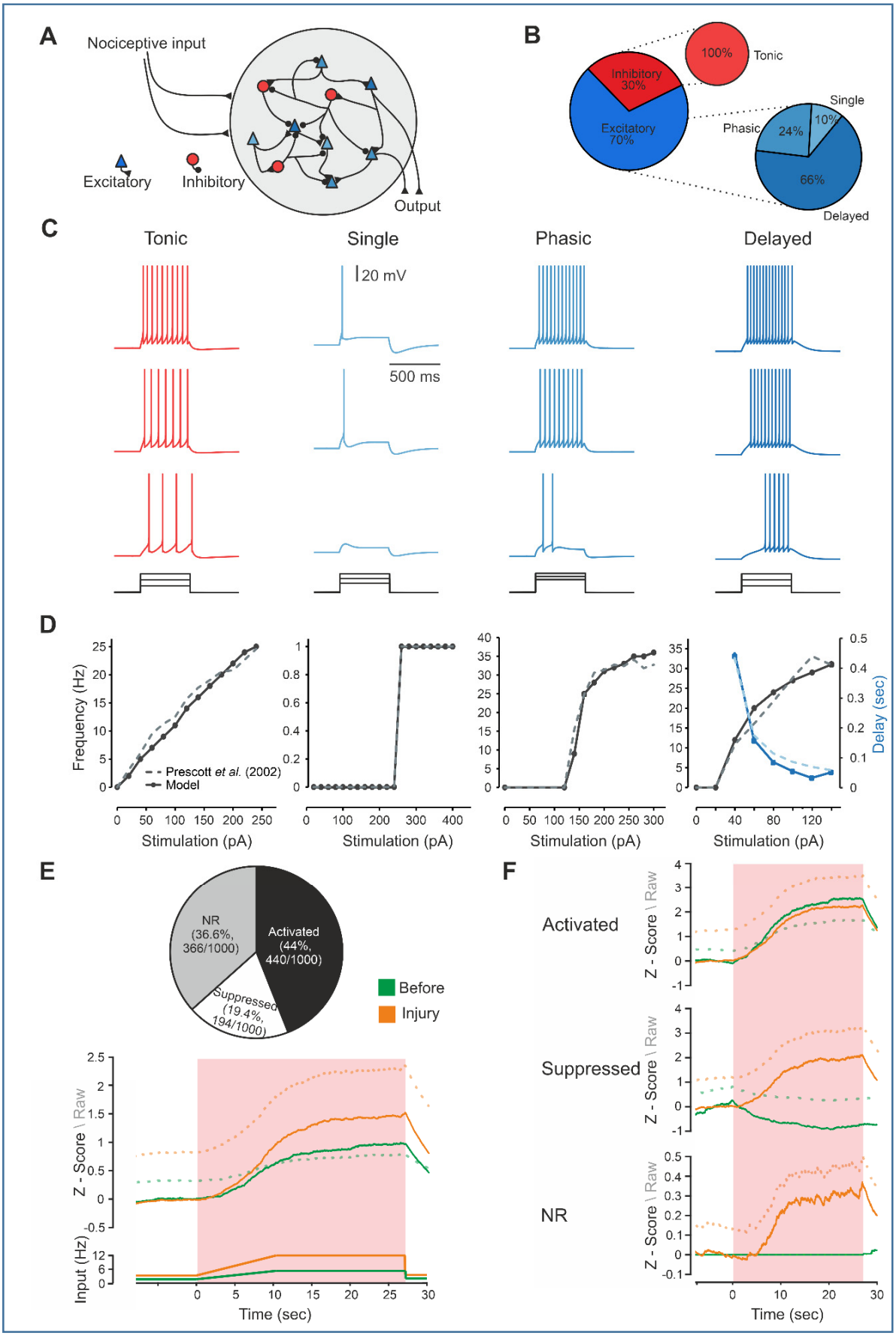
A
Nociceptive input
Excitatory
Inhibitory
Output
B
100%
Tonic
Inhibitory 30%
Excitatory 70%
Single
10%
Phasic
24%
66%
Delayed
C
Tonic
Single
Phasic
Delayed
20 mV
500 ms
D
Frequency (Hz)
Prescott et al. (2002)
Model
Stimulation (pA)
Delay (sec)
E
NR (36.6%, 366/1000)
Activated (44%, 440/1000)
Suppressed (19.4%, 194/1000)
Before
Injury
Z - Score \ Raw
Input (Hz)
Time (sec)
F
Activated
Suppressed
NR
Z - Score \ Raw
Time (sec)

Figure 5. SDH network model predicts the responses of the SDH neurons to noxious heat stimuli in normal and inflammatory conditions. A. Scheme depicting the modeled network, which consists of 1000 neurons including inhibitory (30%, red circles) and excitatory local interneurons and projections neurons (70%, blue triangles) interconnected to each other. The network receives nociceptive input simulated by EPSC-like currents at various frequencies, depending on the modeled conditions. 2 Hz input models the baseline activity, 5 Hz input models the activation of nociceptive neurons by noxious heat in simulated control conditions. The injury conditions are simulated by currents at 4 Hz for baseline and at 12 Hz for evoked activation. **B.** Pie charts showing the percentage of the inhibitory and excitatory cells composing the network and their distribution according to the firing pattern. **C.** Modeled firing of tonic, single, phasic, and delayed firing-type SDH neurons under escalating current clamp steps. Shades of blue represent the modeled excitatory neurons, red represents modeled inhibitory neurons. **D.** Modeled frequency-intensity (*f-I*) curves for each type of neuron (*continuous line*) compared with its respective experimental *f-I* curve from Prescott and De Koninck (2002, *dashed line*). In the delayed neuron, the delay (time to first A.P.) is also compared with the experimental data. **E.** Mean neural activity integration (1000 modeled neurons), in control (*green*) and injury (*orange*) modeled conditions. The solid lines depict the Z-scored changes; the dotted lines depict the unnormalized "raw" changes in the activity integration between the modeled control and injury conditions. *Inset.* The pie chart depicts the fraction of cells that either increased their activity ("activated") or decreased their activity ("suppressed"), following the simulated application of the first noxious heat stimulus, or cells that do not respond to the simulated application of the first noxious heat stimulus ("non-responsive"). **F.** Mean activity of the simulated "activated", "suppressed", and "non-responsive" neurons in simulated control (*green*) and simulated inflammatory conditions (*orange*). The solid lines depict the Z-scored changes; the dotted lines depict the unnormalized "raw" changes in the mean activity integration between the modeled control and injury conditions. Note y-axis expansion for simulated "NR" neurons.

To capture basic spiking features of SDH dynamics, we modeled three well-established types of excitatory neurons with phasic, delayed, and single firing pattern properties and one type of tonically firing inhibitory neuron (Punnakkal et al., 2014, **Figure 5C**). Their modeled firing

properties closely resembled the experimental frequency-current (*f-I*) curves and 'delay curve' of the delayed neurons closely (Prescott and de Koninck, 2002, **Figure 5D**). We simulated the SDH circuitry using a network of 1000 neurons, of them 300 inhibitory neurons, of which all had tonic firing patterns and 700 excitatory neurons of which 25% had phasic, 12.5% delayed, and 62.5% single firing patterns (Punnakkal et al., 2014, **Figure 5B**). In addition to the intrinsic excitatory and inhibitory connections, excitatory and inhibitory neurons also received excitatory inputs with controlled frequency but at random times, simulating nociceptive input from the periphery during baseline and heat stimulation (*see Methods*). To simulate naïve conditions, we stimulated the SDH network model with input currents at 2 Hz and 5 Hz to model baseline and "noxious heat" induced circuit activity, respectively. These stimulation frequencies generate simulated EPSC's frequencies in the SDH model, which were similar to the baseline and evoked SDH EPSC's frequencies reported *in vivo,* respectively (Matsumura et al., 2015; McCoy et al., 2013; Takiguchi et al., 2012; Uta et al., 2019, *see Methods*), thus mimicking the SDH circuit activity before and during noxious stimulation. Tissue injury leads to an increase in both the spontaneous and evoked activity of the peripheral nociceptive neurons (Binshtok et al., 2008; Yarmolinsky et al., 2016). To reflect the increased spontaneous activity of the hyperexcitable primary afferents in the injury model, we increased the frequencies at the baseline conditions to 4 Hz (McCoy et al., 2013, *see Methods*). To simulate the increased evoked activity during the heat stimulus, we increased the input currents frequency to 12 Hz (Bardoni et al., 2019; Hachisuka et al., 2020, *see Methods*). We utilized a calcium imaging-like module, which as in calcium imaging, predicts integration dynamics of electrical neuronal network, to examine whether the simulations qualitatively emulate our experimental data (*see Methods*). Stimulation of the model at the simulated naïve conditions led to an overall increase in neuronal activity (**Figure 5E,** *solid green*). Analysis of the individual modeled cells showed that similar to what we demonstrated *in vivo*, the majority of the cells (44%) increased their activity during the modeled stimulus ("activated"), about 20% decreased their activity ("suppressed"), and the rest did not change their activity during the application of the simulated noxious heat stimulus ("non-responsive," **Figure 5E,** *inset*). Importantly, our model accurately captured changes in the injury conditions when we analyzed Z-scored activity, similarly to the experimental data. Our model showed that the increase in input to the network was sufficient to produce the increase in overall activity ($AUC_{Control}$ = 17.1 ± 1.2 vs. AUC_{Injury} = 26.8 ± 1.6, **Figure 5E,** *solid green and orange lines*). This increase resulted from the activation of the "suppressed" ($AUC_{Control}$ = –16.5 ± 0.71 vs. AUC_{Injury} = 35.8 ± 1.9, **Figure 6F,** *middle panel*, *solid green and orange lines*) and "non-responsive" neurons ($AUC_{Control}$=0 vs. AUC_{Injury} = 5.17

± 0.4, **Figure 6F,** lower panel, *green and orange lines*). Our model also showed that that the increased input to the SDH network did not lead to changes in activation of the "activated" neurons analyzed using Z-score ($AUC_{Control}$ =46.22 ± 1.4 vs. AUC_{Injury} = 40.8 ± 1.9, **Figure 6F,** upper panel, *solid green and orange lines*). Importantly, analyzing the activity of simulated SDH neurons without normalizing to the baseline, i.e., taking into account simulated inflammation-induced changes in the baseline activity, we show that increased input produced more substantial activation of the "suppressed" ($AUC_{Control}$ = 9.8 ± 0.3 vs. AUC_{Injury} = 66.2 ± 2.3, **Figure 5E,** *dotted green and orange lines*) and "non-responsive" cells ($AUC_{Control}$ = 0 vs. AUC_{Injury} = 9.1 ± 0.3, **Figure 5E,** *dotted green and orange lines*) but also substantial activation of the "activated" cells ($AUC_{Control}$ = 34.3 ± 1 vs. AUC_{Injury} = 74.5 ± 2.3, **Figure 5E,** *dotted green and orange lines*).

Altogether our results suggest that SDH circuitry encodes enhanced input from the injured tissue in a complex combinatorial manner, i.e., by changing the activity patterns of the engaged neurons and affecting previously non-responding neurons.

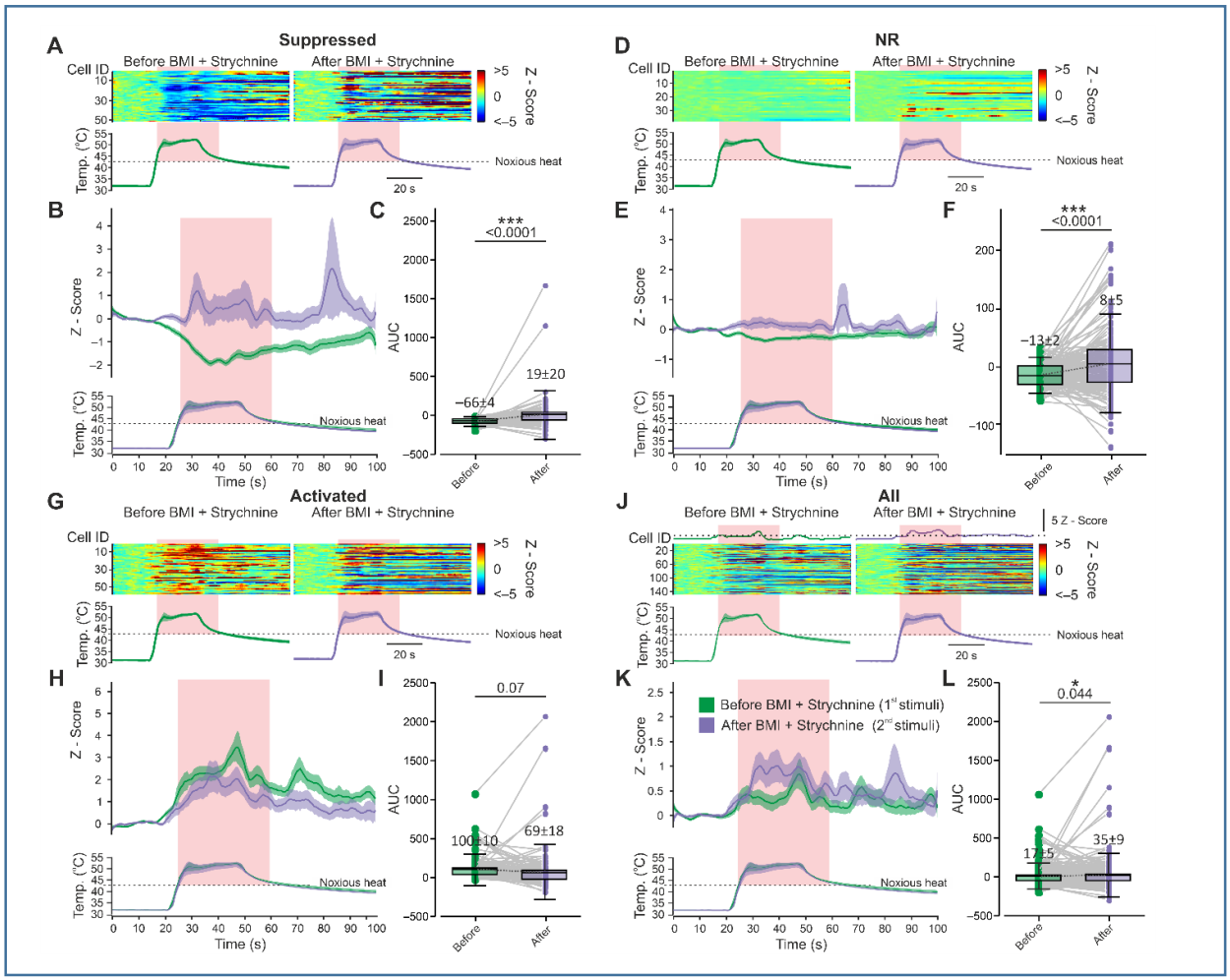

Figure 6. Blockade of the SDH inhibitory synapses mimics the injury-mediated hyperalgesic response of the SDH neurons. A. Representative heat maps of the activity of 52 "suppressed" cells in the same field of view (FOV) during application of noxious heat stimulus to the paw before and 1 hour after treatment with 200 µM bicuculine (BMI) and 40 µM strychnine, to block GABA and Glycine receptors, respectively. The stimuli are shown below the heat maps. The noxious (above 42°C) component of the stimulus is outlined by the pink shadow. Representative of 3 mice. **B.** Changes in intracellular Ca^{2+} (Z-Score, mean ± SEM) in cells which decreased their response to the first noxious heat stimulus ("suppressed") before (*green*) and after (*magenta*) application of 200 µM bicuculine (BMI) and 40 µM strychnine. The noxious (above 42°C) component of the stimulus is outlined by the pink shadow. Note that in the presence of blockers of inhibitory transmission, the second noxious heat stimulus lead to the activation of the "suppressed" cells. n=167 cells from 3 mice. **C.** Box plots and paired individual values of changes in the responses' AUC of the "suppressed" cells before (*green*) and 1 hour after (*magenta*) application of BMI and strychnine. Paired *t*-test, n=167 cells from 3 mice. **D.** Same as *A*, but showing the representative activity heat maps from 38 non-responsive ("NR") cells. Representative of 3 mice. **E.** Changes in the activity of the "NR" cells before (*green*) and after (*magenta*) application of BMI and strychnine. Note that the "non-responsive" cells became activated following the blockade of GABA and glycine receptors. n=148 SDH cells from 3 mice. **F.** Same as *C,* but comparing the AUC of responses to noxious heat of the "NR" cells. Paired *t*-test, n=148 cells from 4 mice. Note a small significant increase in the AUC. Note also the expanded y-axis in order to zoom in the effect of BMI and strychnine on the AUC of "NR" cells. **G.** Same as *A*, but showing the representative activity heat maps from 59 "activated" cells. Representative of 3 mice. **H.** Changes in the activity of the "activated" cells before (*green*) and after (*magenta*) application of BMI and strychnine. Note that blockade of the inhibitory synaptic transmission does not change the response magnitude of the "activated" cells. n=115 cells from 3 mice. **I.** Same as *C,* but comparing AUC of responses to the noxious heat of the "activated" cells. Paired *t*-test, n=115 cells from 4 mice. **J.** Same as *A*, but showing changes in the activity of all recorded cells in the same FOV in one mouse. n=149 cells. Representative of 3 mice. The averaged (means) changes in intracellular Ca^{2+} are shown above the heat maps. The dotted line is aligned to the peak of the mean response before the treatment with BMI and strychnine. **K.** Changes in the activity of all recorded cells before (*green*) and after (*magenta*) application of BMI and strychnine. Note a substantial increase in the overall activity of SDH cells. n=430 cells from 3 mice. **L.** Same as *C,* but comparing the AUC of the overall responses to the noxious heat of all

recorded cells. Paired *t*-test, n=430 cells from 4 mice. The data points shown in *C, F, I,* and *L* were collected and analyzed over the time of the noxious part of stimulus (*see Methods*). Box plots depict the mean and 25 and 75 percentiles, and the whiskers depict SD. Numbers above the boxes are means ± SEM. For the comparison of changes in the responses' mean amplitude, see **Supplementary Figure 7**.

Our results show that the input from the periphery during noxious heat stimuli under naïve conditions produces a reduction in the activity "suppressed" cells. These results suggest the existence of an inhibitory drive during noxious heat stimuli in the SDH circuity. Furthermore, we showed that in hyperalgesic conditions, the noxious heat stimuli lead to a decrease in the activity suppression of the "suppressed" cells and activation of a subset of previously "non-responsive" cells, thus inducing the overall activation of the SDH circuitry, suggesting that the inhibitory drive under this condition is reduced. To test whether disinhibition is sufficient for producing the change caused by the abnormal input from the injured tissue, we examined the response of SDH cells to noxious heat stimuli following the blockade of inhibitory synaptic inputs at the SDH. To that end, we tested the response to noxious heat stimuli before and after local application of bicuculine (BMI, 200 μM) and strychnine (40 μM) to block GABA and glycine receptors, respectively. These concentrations were used in order of magnitude above of previously used to assure that the pharmacological reagents will reach the neurons at high concentrations through the plastic imaging cover window (Narikawa et al., 2000; Yamanaka et al., 2015). Application of BMI and strychnine reversed the activity suppression of the "suppressed" cells (**Figure 6A, B, Supplementary Figure 7A)** and led to an overall activation of the "non-responsive" cells (**Figure 6E, F, Supplementary Figure 7C**). These results support the statement that in naïve conditions, a decrease in the activity of the suppressed cells or activity silence of the non-responsive cells in response to the application of the noxious heat stimuli could result, at least partially, from the inhibition of the "suppressed" and "non-responsive" "to be" cells. Importantly, the decrease in the activity suppression together with activation of the non-responsive cells was sufficient to increase the overall activity of the SDH circuitry (**Figure 6G, H, Supplementary Figure 7D)** since the activity of the "activated" cells was not affected by the blockade of inhibition (**Figure 6C, D, Supplementary Figure 7B)**. Thus, the response pattern of SDH neurons in response to noxious heat stimulus applied to the injured skin is similar to the response to the noxious heat stimulus when the SDH inhibition was reduced. These results suggest that changes in the activation pattern of the pain-related

SDH network, which encode thermal hyperalgesia, may result at least in part from the acute decrease in the inhibitory drive. Notably, a decrease of the inhibitory inputs (70%) applied to the SDH network model to simulate the blockade of inhibition led, similarly to what we demonstrated *in vivo,* to the increase in the overall evoked integrated activity compared to control AUC (17.1 ± 1.2 vs. 30.3 ± 2.1, **Supplementary Figure 8A,** *magenta*). The model shows that disinhibition caused an increase in the activation of the activated cells ($AUC_{Control}$ = 34.3 ± 1 vs. $AUC_{Disinhibition}$ = 57.8 ± 1.5, **Supplementary Figure 8B,** *upper panel*, *magenta*) and a decrease in the activity suppression of the suppressed cells ($AUC_{Control}$ = –16.6 ± 0.7 vs. $AUC_{Disinhibition}$ = –5.3 ± 0.7, **Supplementary Figure 8C,** *middle panel*, *magenta*). Moreover, under these conditions "non-responsive" neurons of the model became activated ($AUC_{Control}$ = 0 vs. $AUC_{Disinhibition}$ = 3.4 ± 0.2, **Supplementary Figure 8D,** *lower panel*, *magenta*).

The abovementioned results show that the blockade of the inhibition might indeed unmask the activation of the non-responsive cells and reduce the suppression of the suppressed cells activity, thus leading to the increase in the overall activity. On the other hand, our model predicts that the SDH network cytoarchitecture by itself is prone to disinhibition-like changes. We show that the increased input from the peripheral afferents conferred upon the SDH network is sufficient to reduce the suppression and activate non-responsive cells without accompanying changes in the inhibitory transmission (**Figure 5E-F**).

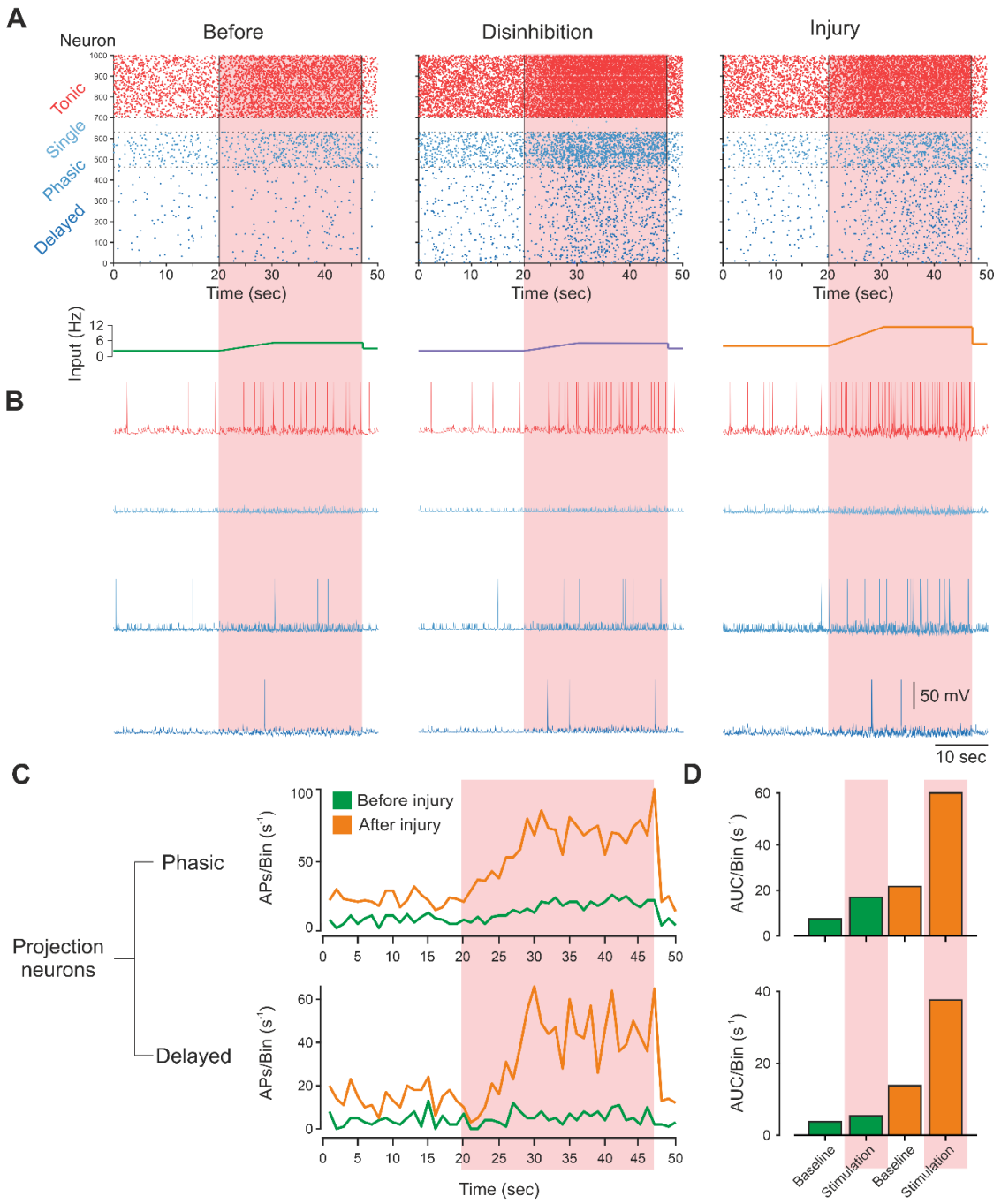

Figure 7. Modeled inflammatory conditions predict an increase in the firing of excitatory SDH neurons. A. Raster plots of 1000 spiking neurons in modeled control, disinhibition, and injury condition-like states. Neurons are grouped by their intrinsic firing patterns and colored according to their excitatory (*delayed, phasic, single in shades of blue*) or inhibitory (*tonic in red*) properties, respectively. The stimulation frequency is depicted under each plot. **B.** Example traces of each type of neuron from the modeled networks presented in *A*. **C.** Summation of the number of action potentials fired (1s/bin) of phasic and delayed firing

excitatory neurons during the stimulation time shown in *A*, in simulated normal (*before the injury, green*) vs. injury conditions (*after injury, orange*). **D.** Bar graphs depict AUC from the plots shown in *C*. Note the increase in activity during simulated noxious stimulation compared to baseline, and substantial increase in response in the simulated injury model.

Our results suggest that the SDH network model simulates well the behavior of the pain-related spinal cord circuitry, at least at the examined parameters, thus providing a sufficient basis to use this model for more complex predictions of the SDH network behaviors. Our *in vivo* results demonstrated that "noxious heat" stimuli in naïve and inflamed conditions increase the overall neuronal activity. However, it is unclear whether this increase is translated into increase in the excitatory output of the SDH network. Our data imply that the increase in overall activity may involve increased activity of both excitatory and inhibitory neurons, which may have unpredictable net effects. We, therefore, used the SDH network model to predict how changes in the input affect the activity of individual excitatory and inhibitory neurons composing the SDH network (**Figure 7A, B**), focusing on the population of excitatory neurons with either phasic or delayed firing patterns as they are strongly associated with the projection neurons (Grudt and Perl, 2002; Li et al., 2000; Ruscheweyh et al., 2004). The analysis of the firing of the individual neurons divided into subcategories according to their network effect (excitatory/inhibitory) and their firing pattern show that both disinhibition and simulated injury-models lead to increased firing of the tonic inhibitory neurons, they also lead to the increased firing in excitatory phasic and delayed neurons (**Figure 7A, B**). We then compared the firing of the excitatory phasic and delayed neurons in simulated naïve conditions and simulated injury conditions. Our model predicts that in naïve conditions, the excitatory phasic but not delayed neurons increase their firing slightly (**Figure 7C, D,** *upper and middle panels*, *green*), while in the simulated injury conditions, both excitatory phasic and delayed neurons substantially increase their firing (**Figure 7C, D,** *upper and middle panels*, *orange*). Considering that the projection neurons are excitatory neurons with either phasic or delayed firing pattern (Grudt and Perl, 2002; Li et al., 2000; Ruscheweyh et al., 2004) the substantial increase in firing of these excitatory neuronal types in response to the same noxious heat stimulus suggest that inflammation-induced increased input to the SDH produces increased output from the SDH network. The increased SDH output in response to the same noxious heat stimulus changes noxious heat stimulus perception which is relayed to higher brain centers generating pain hyperalgesia.

Discussion

A fundamental question in understanding pathological pain is what are the changes occurring within CNS neuronal networks, which lead to increased response to noxious heat stimuli and thereby amplifying pain (Kuner, 2010). Here we reveal how noxious thermal stimuli applied in inflammatory conditions are represented in the SDH *in vivo* leading to enhanced noxious thermal perception. Our data suggest that in normal conditions, activation of peripheral nociceptive neurons triggers an inhibitory drive leading to silencing and even activity suppression of SDH neurons. Inflammation-induced enhanced input from nociceptive neurons reduced the effect of this inhibitory drive, thus leading to an overall increase in the network activity. Our computational model predicts that this functional change in SDH activity might lead to hyperalgesia by substantially increasing the activity of SDH excitatory interneurons and projection neurons.

The CNS plays a critical role in integrating and processing sensory input, and it is constrained by how sensory information is represented by primary afferent neurons. Activation of specific receptors and ion channels in peripheral nerve endings by chemical, mechanical or thermal stimuli triggers the action potential firing generating the output of nociceptive neurons towards the SDH (Barkai et al., 2020; Goldstein et al., 2019; Julius and Basbaum, 2001; Waxman and Zamponi, 2014). These input-output parameters of peripheral nociceptive neurons are altered under pathological conditions such as inflammation, which leads to changes in nociceptive intrinsic excitable properties, thus altering the transmission code by changing the rate and timing of the firing (Barkai et al., 2020; Binshtok et al., 2008; Cho et al., 2016; Yarmolinsky et al., 2016). Here we utilized *in vivo* 2PLSM imaging of a large population of neurons to examine how SDH circuitry changes its responses to abnormal peripheral inputs in inflammatory conditions. We show that application of the noxious thermal stimuli leads to the increase in activity of only a fraction of neurons. We show that about 30% of the recorded neurons remain silent following the application of noxious heat stimuli. A previous study showed that the application of noxious thermal stimuli leads to the activation of a fraction of SDH neurons and that this fraction increases with the increase in stimulated temperature (Ran et al., 2016). The number of the responding neurons culminated at about 80% when the paw was stimulated with a noxious 50°C heat (Ran et al., 2016). Here we show that noxious heat stimuli applied during inflammation convert some of the silent neurons into active neurons, thus increasing the overall number of activated neurons. The underlying mechanism of this inflammation-mediated increase in responding neurons may involve unmasking of new

peripheral-to-central connections (Matsumura et al., 2015) or activation of silent thermosensitive neurons (Yarmolinsky et al., 2016). It is also feasible that SDH neurons which do not respond to application of noxious heat stimuli are silenced by noxious-stimuli-triggered inhibition. We showed that the noxious heat stimuli applied in the hyperalgesic conditions result in the de-suppression of cells suppressed during the application of noxious heat stimuli before inflammation induction. These results suggest that noxious heat stimuli in normal condition trigger the inhibitory drive which suppresses the activity of some neurons and possibly prevent the activation of other, non-responsive neurons. This noxious-stimuli-mediated inhibition could result from activation of tonically active local inhibitory neurons and also from descending inhibition, triggered by noxious heat stimuli (Ossipov et al., 2010; Todd, 2010). Our model containing only local inhibitory connections from local inhibitory interneurons predicts that activation of local inhibitory SDH neurons by the noxious-like input in normal conditions is sufficient by itself to suppress and silence the activity of modeled SDH neurons. Our results also demonstrate that enhanced input from the periphery leads to "disinhibition-like" changes resulting in the de-suppression of the suppressed neurons and activation of the silenced neurons, thus contributing to the overall increase in the activity of the SDH network.

What could be the origin of this disinhibition? Disruption of the chloride equilibrium or changes in the neuronal excitability and their synaptic efficacy were proposed as a principal mechanism underlying nerve-injury-mediated tactile allodynia (Balasubramanyan et al., 2006; Coull et al., 2003; Schoffnegger et al., 2006; Zhang et al., 2018). The majority of these requires activation of complex cascades thus it requires a time scales of many hours (Coull et al., 2005; Hughes et al., 2020). Our experiments demonstrate the disinhibition-like changes of the SDH circuit that occur within 1 hour following injury. Therefore, it could be that the acute hyperalgesia we observed is mediated via a different, much more rapid mechanism. We hypothesized that abnormal input from the periphery disrupts the excitation-inhibition balance of the SDH circuitry thus leading to the disinhibition-like changes. SDH circuitry consists of approximately 30% inhibitory neurons, the rest of the neurons composing the SDH network are excitatory interneurons and projection neurons (Peirs et al., 2020; Polgár et al., 2013). While excitatory neurons possess either delayed, phasic or single spike firing patterns (Prescott and de Koninck, 2002; Punnakkal et al., 2014) inhibitory neurons respond to the input by amplified output, i.e., with tonic firing (Prescott and de Koninck, 2002; Punnakkal et al., 2014) thus balancing the excitatory drive. It is plausible that enhanced input from the hyperactive

peripheral nociceptive neurons would promote primarily excitatory drive. Stronger input into more abundant excitatory neurons may lead to an excitatory drive which would overcome tonic output of fewer inhibitory neurons, thus leading to the disruption of excitatory-inhibitory equilibrium towards more excitation and to consequently a stronger activation of "suppressed" and "non-responsive" neurons. It also shows that stimulation of the modeled network by inflammation-like increased input leads to increased activity of the "suppressed" neurons and an increase in the number of activated neurons by converting some of the non-responsive neurons into active ones. These computational results predict that inflammation-mediated abnormal input conferred upon unique intrinsic SDH network cytoarchitecture is sufficient to disrupt the excitation-inhibition balance by increasing the excitatory drive. The unbalanced excitation could, by overcoming the inhibitory effect on the "suppressed" neurons and unmasking inhibitory-mediated silence of "non-responsive" neurons, lead to an overall increase in the activity of the SDH network.

The alternative explanation for the inflammation-mediated disinhibition-like changes in the SDH network could be a decrease in inhibitory transmission. Our experimental results demonstrated that blockade of GABA and glycine receptors mimics the inflammation-induced SDH network activity changes, emphasizing yet again the role of spinal cord inhibitory transmission in controlling the output of the SDH network (Braz et al., 2014; Bráz et al., 2012; Hughes et al., 2020; Takazawa and MacDermott, 2010). If the latter is the case, the effect of disinhibition would primarily enhance the activity of the excitatory SDH neurons as they rely more strongly on the inhibition to counterbalance the strong excitatory inputs they receive (Lee et al., 2019). Although the majority of changes leading to disinhibition in the spinal cord requires time and they observed mostly after nerve injury or persistent inflammation (Hughes et al., 2020; Moore et al., 2002; Takazawa and MacDermott, 2010), it is also plausible that right after the injury hyperexcited peripheral axons, similarly to the injured axons in nerve injury models (Coull et al., 2005), release a variety of mediators towards the SDH neurons, affecting the intrinsic excitability of inhibitory neurons. Thus, although our model predicts that the increase in SDH network activity can occur without changes in inhibitory synaptic transmission, just by virtue of the architecture of the SDH neuronal connections and their firing properties, it is feasible that the combination of both - inflammation-induced decrease in inhibition and SDH network mediated excitatory-inhibitory disbalance - encodes the abnormal input from the peripheral nociceptive neurons.

Our data demonstrate changes in activity of cells according to their response pattern to noxious heat stimuli in normal conditions: activated, suppressed, non-responsive. This classification cannot predict the overall effect of the change as it does not account for the excitatory or inhibitory nature of these neurons. To interpret our data in this context, we built a realistic LIF neural network model of 1000 excitatory and inhibitory SDH neurons. The activity patterns of these simulated neurons we based on whole-cell patch-clamp data from dorsal horn firing properties from literature (Peirs et al., 2020; Polgár et al., 2013; Prescott and De Koninck, 2002; Punnakkal et al., 2014). Our model was able to mimic the experimental results and recapitulate the same patterns of activity of the SDH neurons: activated, suppressed and non-responsive. Therefore, we further utilized this model to make more advanced predictions. We examined the net effect of the inflammation-mediated changes now according to the specific firing and synaptic parameters of the neurons. While our conclusions were robust using several combinations of parameters, we do not claim that the model is realistic in an absolute sense. Its purpose is to demonstrate the plausibility of our interpretation and the proposed experimental model with parameter values constrained by the literature. Based on these assumptions, our model predicts that increased input from peripheral nociceptive neurons leads to overall modification in the SDH network activity pattern, converging into substantial increased firing of the excitatory projection neurons, thus leading to inflammatory hyperalgesia.

In summary, here we introduced an approach which allows studying the SDH network representation of activity changes underlying pathological pain. By combining *in vivo* imaging with a network model of inflammatory pain, our data provide insight into the analysis of the representation of inflammatory hyperalgesia by spinal cord neurons. We show that inflammation-mediated nociceptive hyperexcitability is encoded by the acute changes in excitation-inhibition balance within the SDH, leading to a decrease in inhibition of activity and an increase in the number of activated neurons. These acute changes in the activity of pain-related spinal cord circuitry, by responding with higher excitatory output to the same noxious heat stimuli, might underlie changes in the perception of the noxious heat stimuli, thus leading to inflammatory hyperalgesia.

Acknowledgements

We would like to thank Dr. Xioake Chen from Department of Biology, Stanford University and Dr. Qian Wang from Chen's lab for training us in performing 2PLSM from SDH. We would also like to thank R. Sharon for the assistance with image registration performance.

***Funding sources*:** Support is gratefully acknowledged from the Canadian Institute of Health Research (CIHR), the International Development Research Centre (IDRC), the Israel Science Foundation (ISF) and the Azrieli Foundation - grant agreement 2545/18; Israeli Science Foundation - grant agreement 1470/17; the Deutsch-Israelische Projectkooperation program of the Deutsche Forschungsgemeinschaft (DIP) grant agreement B.I. 1665/1-1ZI1172/12-1 and Sessile and Seymour Alpert Chair in Pain Research.

Author contributions: Conceptualization, O.B. and A.M.B.; Methodology O.B., R.B. and A.M.B.; Investigation, O.B., R.B., B.K, S.L. and A.M.B.; Writing - Original Draft, O.B., B.K, S.L. and A.M.B.; Funding Acquisition, A.M.B.; Supervision, A.M.B.

Declaration of Interests: The authors declare no competing interests.

Materials and Methods

Animals

Young adult (4-6 week) C57BL/6J female mice were used for calcium imaging. According to Ran et al., (Ran et al., 2016), the female mice were used in this study for easier tissue removal during surgery and minimization of light intensity attenuation. Mice were group-housed on a 12-h light cycle and were randomly assigned for experiments. All procedures were conducted in accordance with the guidelines and approved by the animal ethics committees of the Hebrew University of Jerusalem (MD18-15608).

Surgery

The surgical approach was adapted from a method previously reported (Johannssen and Helmchen, 2010; Ran et al., 2016). Animals were anesthetized with urethane (2 mg g^{-1}), delivered by 2 i.p. injections separated by 30 min. Surgery started 30 min after the second urethane injection. Corneal reflex was examined throughout the experiment, and up to 0.6 mg g^{-1} additional urethane might have been given to animals with a corneal reflex response. A tracheotomy was then performed. Core body temperature was maintained at 36°C ± 1°C with a closed-loop heating system throughout surgery and imaging. The right hind limb was gently shaved with hair removal cream. Paravertebral muscles at vertebrae level T10–L1 were retracted, and spinal clamps (STS-A, Narishige) were used to clamp the exposed vertebral column and stabilize the preparation. A dorsal laminectomy was performed at vertebra level T12 to expose the spinal cord. A custom-designed plastic chamber was placed around the vertebrae and was sealed with agarose to create a watertight compartment for the use of a water immersion objective. The exposed spinal cord was kept at a stable temperature with normal Ringer solution (in mM: 135 NaCl, 5.4 KCl, 5 HEPES, 1.8 $CaCl_2$; pH 7.2, 30–32 °C). The dura mater was carefully removed with a fine needle, and the animal was rotated around the longitudinal axis by ~30 degrees for imaging. Blood flow through the central vessel was closely monitored as an indicator of tissue health throughout the experiment.

Dye injections

Neurons in the superficial laminae of the dorsal horn were bulk-loaded with the Oregon Green 488 BAPTA-1 AM (OGB, Invitrogen) under 2PLMS as described previously (Ran et al., 2016). We used glass pipettes with 2–3 µm tips to inject a solution containing 1 mM OGB and 50 µM Alexa Fluor 594 or for some experiments 0.25mg/ml µM Sulforhodamine 101 (SR-101)

(Nimmerjahn et al., 2004), 10% dimethyl sulfoxide and 2% (w/v) Pluronic F-127 in Ca^{2+}/Mg^{2+} free pipette solution (in mM: 150 NaCl, 2.5 KCl, 10 HEPES; pH 7.4). The dye solution was maintained at ~0 °C before filtered with a 0.22 µm centrifuge filter (Millipore) and loaded into a glass pipette. The pipette tip was targeted 70–130 µm below the surface of the spinal cord, about 200 µm lateral to the central vessel. Spinal neurons were bulk-loaded for about 3 min by applying 900 ms pulses of 15–25 psi to the pipette to pressure-eject the dye at 3 or more sites approximately 200 µm apart from each other. After dye injection, the imaging site was covered with a No. 0 glass coverslip pre-cut to fit inside the custom chamber, sealed with 2% agarose in Ringer solution, except in the experiments using synaptic blockade pharmacology, in which the imaging site was covered with a plastic coverslip with an access pore for drug application.

2PLMS imaging

Two-photon calcium imaging experiments were performed as described in Ran et al. (Ran et al., 2016). Briefly, with a two-photon microscope (Zeiss) using a Zeiss 20× water-immersion objective (I.R., N.A. = 1.0) with 1× optical zoom. This provided a 438 × 438 µm field of view (FOV) that was scanned at 2 Hz and recorded as a series of 256 × 256 pixels FOV. Both SR-101 and OGB were excited using an 810 nm Ti: sapphire laser (Chameleon, Coherent). The SR-101 fluorescence was separated from the OGB fluorescence using a dichroic mirror (562 nm, Semrock Inc., Rochester, NY, USA). Fluorescence emissions were detected simultaneously by two non-descanned photomultiplier tubes with a 542/50 nm filter (Semrock) for 'green' fluorescence emission and a 617/73 nm filter (Semrock) for 'red' fluorescence emission.

The mouse's right hind limb paw of the mouse was placed on a custom-designed 1cm X 1cm Peltier device (**Figure 1A**), with an aluminum tape wrapped around the dorsal side of the paw to keep the paw stretched and stable. The Peltier element was held at a baseline temperature (B.T.) of 32°C before noxious heat stimulus were applied by injecting current with a D.C. power supply (TTi PL-303) digitally tuned and controlled with Axon MultiClamp device and pClamp10 software.

For each trial, the spinal cord was imaged for 20 s at the baseline temperature to obtain baseline fluorescence and noise before applying noxious heat stimulus. 2 trials of each stimulus were imaged in each spinal FOV. Mild burn injury was induced by delivering a hyperalgesia-

inducing (50-65°C) thermal stimulus using the same stimulation source as all other temperature stimuli.

Image analysis

Videos were imported into ImageJ for concatenation. Movement corrections were performed using a custom-built Matlab code available upon request. Ca^{2+} imaging analysis was performed using the MIN1PIPE calcium imaging signal extraction pipeline (Lu et al., 2018), which we used for background removal, automatic ROI identification, and signal extraction based on spatial and temporal properties of individual units. A priori structural element estimate was initialized at 5 pixels to seed ROI detection. An average of 145 ROIs was detected in a recording. For population analyses, we calculated Z-scores for the neuronal responses using the mean and the standard deviation of the 20 s baseline period preceding stimulation onsets per each recording session (before vs. after). All traces were smoothed prior to analysis using Matlab's default Smooth function, with a moving average filter with span = 10. Responses were classified by their 'before' traces as "activated" or "suppressed" by the sign of the integral (+/−) during stimulation and if during that period their intensity passed 2 S.D. or −2 S.D. threshold in at least three consecutive time points. Neuronal signals that were not classified as "activated" or "suppressed" and did not pass the threshold value were classified as "non-responsive." Raw images and individual neuronal responses were visually observed. Experiments or neurons with failed image registration and irregular motion artifacts (because of thermal stimulus-induced reflex paw movement due to insufficient anesthesia) were excluded.

The data points for AUC and mean amplitude were collected and analyzed only over the time of the noxious part of stimulus from 42ºC and until 50ºC, right after the heat ramp was stopped and the heat started to decrease ('noxious period'). The data were calculated relative to the baseline obtained before the relevant imaging session. No comparison between the baselines of the different recording sessions of the same experiments was performed due to time-dependent sample movement and decay in fluorescence. The area under the curve (AUC) and mean amplitude were measured for each cell. Mean amplitude was measured as the mean activity during the baseline period subtracted from the mean activity during the 'noxious period.'

Astrocytes activity analysis. Cells that exhibited both green (OGB-AM) and red (SR-101) fluorescence with a confidence overlap of 80% of the detected neuron/astrocyte surface were tagged as astrocytes. Their activity was then analyzed as for neurons (*see above*).

Behavioral experiments

Burn injury induction. Hyperalgesia-inducing heat injury was applied to the glaborous skin surface of the mice hind paw with the exact same procedure used in the two-photon experiments by applying 20s 50 to 65°C thermal stimulus using the Peltier apparatus described above. The injury protocol was delivered while the animals were deeply anesthetized with isoflurane, to minimize animal suffering and stress. Animals were then returned to their home cages for 1 hour of injury development and to allow full recovery from anesthesia before returning to the test environment chambers.

Warm surface open field test. Burn injury was induced as described above. Animals were placed on a 41ºC, under-noxious heated metal plate surrounded by white plastic walls. Plate size was 20cm x 20 cm box arena. The box was cleaned with ethanol and water before each mouse was introduced to the arena. Animals were recorded during behavior time (5 min) for post-hoc analysis. To assess mobility distance traveled was analyzed with TrackRodent open-source video tracking software (Netser et al., 2019). Mice were not introduced to the arena before the experiment.

Hargreaves radiant heat test. Two groups ("control" and "injury") of 6 mice were habituated to handling and experimental procedures for 48 hours before the testing. The mice were habituated to the test environment for 24 hours in Plexiglas chambers and the experimental surfaces before the behavioral tests. The behavioral baseline was obtained by 2 preliminary measurements on the day before and the first day of the experiment. Thermal sensitivity was determined using paw withdrawal latency (PWL) determined with a Hargreaves device (Ugo Basile, Varese, Italy). A radiant heat source was applied to the plantar hind paw at IR=30% intensity. A 20-seconds cutoff time was used, to avoid tissue damage.

Tissue thickness measurements. For tissue swelling analysis, a digital micrometer (Mitutoyo) was used to measure the thickness of the plantar area before and at defined time points after injury induction. Thickness increase was calculated as differences from baseline measurements.

Computational model

The computational model is composed of 1000 neurons, with 300 inhibitory (Ni, 30%) and 700 excitatory (Ne, 70%) Conductance-based Adaptive Exponential (CAdEx) integrate-and-fire neurons (Górski et al., 2021; Peirs et al., 2020; Polgár et al., 2013). 100% of the inhibitory

neurons had a tonic firing pattern. Excitatory neurons were divided into three classes of firing patterns: delayed (66%), phasic (24%) and single (10%) (Punnakkal et al., 2014). Neuronal firing patterns were manually tuned to fit with SDH neuron firing properties according to Prescott et al. (Prescott and De Koninck, 2002) (**Table 1**, **Figure 6C, D**). The aim of the single neuron model was to recapitulate the experimental firing properties of the main classes of SDH neurons. Experimental frequency-current (*f*-I) and delay curves were manually extracted using WebPlotDigitzer.

The equations of a single CAdEx model neuron was as follows:

$$C\frac{dV}{dt} = g_L(E_L - V) + g_L\Delta_T exp\left(\frac{V - V_T}{\Delta_T}\right) + g_A(E_A - V) + I_s + I_{ext}$$

$$\tau_A\frac{dg_A}{dt} = \frac{\bar{g}_A}{1 + exp\left(\frac{V_A - V}{\Delta_A}\right)} - g_A$$

With the following after-spike reset mechanism

$$If\, V \geq V_{AP}\ then \begin{cases} V \rightarrow V_R \\ g_A \rightarrow g_A + \delta g_A \end{cases}$$

Where C represents the membrane capacitance, E_A is the reversal potential of adaptation conductance, V_{rest} is the membrane's resting potential, V_A is the subthreshold adaptation threshold, Δ_A is the slope of subthreshold adaptation. V_T is the spike threshold and Δ_T is the slope of the spike initiation; g_L is the leak conductance.

Table 1. The parameters of CAdEx model for firing patterns shown in **Figure 6C**

	C $[pF]$	E_A $[mV]$	V_{rest} $[mV]$	V_A $[mV]$	Δ_A $[mV]$	V_R $[mV]$	V_T $[mV]$	δg_A $[nS]$	$\bar{g}_A$ $[nS]$	g_L $[nS]$	τ_A $[ms]$	Δ_T $[mV]$	τ_{ref} $[ms]$
Tonic	*300*	*-70*	*-60*	*-45*	*5*	*-55*	*-52*	*7*	*2*	*1*	*40*	*2*	*5*
Phasic	*240*	*-70*	*-60*	*-50*	*5*	*-55*	*-49.1*	*-1*	*10*	*8*	*200*	*2*	*20*
Delayed	*370*	*-65*	*-65*	*-60*	*-7*	*-55*	*-55*	*0*	*5*	*2*	*20*	*2*	*18*
Single	*400*	*-150*	*-60*	*-50*	*5*	*-55*	*-50*	*3*	*10*	*12*	*200*	*2*	*5*

An action potential is initiated when V reaches V_T, and the exponential term escalates fast. When it reaches the detection limit ($V_{AP} = 0\ mV$), the membrane potential is set to 30mV and

reset to V_R, and then goes through a refractory period of τ_{ref} linearly graduating (slope = $1 \cdot 10^{-5}$). g_A is incremented by a quantal conductance δg_A after each spike. I_s and I_{ext} represent the currents received from synaptic and external (nociceptive) inputs.

Simulations were computed with time steps of 0.05 ms and lasted 50 second. Model source codes will be available on the ModelDB sharing repository.

Synapses. Post-synaptic potentials (PSPs) amplitude were determined by the spikes emitted by the pre-synaptic neurons in the LIF network. All of the synaptic connections between neurons were unidirectional (Lu and Perl, 2003, 2005) with a connectivity weight, randomly chosen with a 0-to-1 distribution and a mean of 0.5. In every pair of neurons, the unidirectionality (pre- or post-synaptic neuron) was randomly assigned. Input current's connectivities for the excitatory populations (E → E, I → E) were enhance by 2.5-fold (Lee et al., 2019).

The synaptic connection weights between the neurons are given by the matrix S = (s_{ij}), so that firing of the jth neuron instantaneously changes variable I_s of the ith neuron ($I_s^i(t)$) by s_{ij}:

$$I_s^i(t) = \sum_j s_{ij}$$

$$s_{ij} = \theta_{E/I} \cdot Ws_{ij}^{E/I} \cdot rand(0,1)$$

$$\theta_{E/I} = \begin{cases} 1\ if\ excitatoty\ (E) \\ -1\ if\ inhibitory\ (I) \end{cases}$$

Synaptic weights were tuned to fit neuron-to-neuron pairing experiments (François et al., 2017)) between a pre- (index *i*) and post- (index *j*) synaptic neuron. The excitatory\inhibitory (E\I) weights were $= 5 \cdot 10^{-9}$ and $Ws_{ij}^{I} = 2.5 \cdot 10^{-9}$; where neuron i synaptically projects to neuron j, for excitatory and inhibitory neurons respectively. In the excitatory case, a single A.P. firing from neuron *i* with a synapse to neuron *j*, lead to an EPSP of ~ 0.5 - 1.5mv. In the inhibitory case, a single A.P. lead to an IPSP of ~1-3mV, values within experimental range values (Lu and Perl, 2003). The sign of the synaptic weight (+/−) was according to E/I characteristic of the neuron respectively.

External input. The synaptic weight for the external input to excitatory or inhibitory SDH neurons was $W_{ext} = 50 \cdot 10^{-9}$ and lead to an EPSP of ~13 mV (or lead to A.P. firing) agreeing with experimental ranges (Kohama et al., 2000). To cause a biologically-like inconsistency between synapses, a random variable, ranging between 0 to 1, was introduced to each synaptic

connection. All external inputs' synaptic weights were positive, as nociceptors are excitatory neurons.

Spontaneous activity of superficial dorsal horn neurons has been reported in several in vivo preparations (Hentall, 1977; Kumazawa and Perl, 1978; Sandkühler and Eblen-Zajjur, 1994) as well as *in vitro* preparations(Li and Baccei, 2011; Lucas-Romero et al., 2018; Roza et al., 2016).

To replicate the experimental conditions, we tuned the external input frequencies to published literature EPSC event frequency in SDH neurons. A 2 Hz A.P. input rate for control baseline conditions produced a 7.16 ±0.01 Hz EPSC frequency, and 4 Hz A.P. input rate for injury baseline conditions produced a 21.93 ±0.04 Hz EPSC frequency, fitting published literature for control vs. inflammatory model conditions (Matsumura et al., 2015; McCoy et al., 2013; Takiguchi et al., 2012; Uta et al., 2019)

For evoked activity (mimicking heat stimulation in the experimental procedures) in control conditions, the external input frequency was ramped (7 sec, **Figs. 6, 7**) to 5Hz producing a 17.42 ±0.06 Hz EPSC frequency to reach a capsaicin-mediated elevation of EPSC frequency in control conditions in SDH neurons (McCoy et al., 2013). For injury conditions, we increased the external input to 12 Hz, leading to a 61.52 ±0.14 Hz EPSC frequency, reaching the higher rates mentioned in published literature (Bardoni et al., 2019; Hachisuka et al., 2020). 70% of randomly chose SDH neurons received external inputs (Wang et al., 2018).

For mimicking the disinhibition model, we attenuated the inhibitory synaptic weights to 30% of their original weight values, a value which allowed the maximal inhibition without triggering continuous spontaneous activity reaching the simulations A.P. frequency saturation values.

Modeled evoked changes in intracellular Ca^{2+}. To mimic calcium imaging integration signals we used a simplified process of convolution between each neuron's membrane potential output trace and the following exponential-decay function:

$$\xi(0) = 0$$

$$\xi(t > 0) = 1 \cdot \exp(-{}^{t}/_{\tau_\xi})$$

Where $\tau_\xi = 5\ sec$ is the integration time constant, tuned to mimic the calcium imaging traces of the experimental control traces (Figure 1) and then tested on the computational injury and disinhibition models. Each neuron's intensity integration was then Z – scored with a base line

of 7 seconds. We allowed a 13 second period for the cells to reach a stable baseline. We then classified the neurons to activated, suppressed and non-responsive by comparing the mean intensity integration between baseline and stimulus. When mean intensity during stimulation was higher or lower than baseline, neurons were classified as activated or suppressed, respectively. When equal, they were classified as non-responsive.

Reagents

GABA and Glycine inhibitors (Sigma, St. Louis, MO) were applied by superfusion on top of a custom-made plastic coverslips with 3 drug application access pores. Because the coverslip limited the drug diffusion and application time, we used 10 times higher concentrations than previously used in electrophysiological experiments (Narikawa et al., 2000; Yamanaka et al., 2015).

Statistical analysis

Statistical analyses were performed using Prism 7 (GraphPad). Quantitative data were expressed as the mean ± SEM. We did not perform a power analysis as the proposed experiments are novel, and cannot estimate the effect size, however sample sizes in the current study were similar to previous reports(Kohro et al., 2020; Ran et al., 2016). Mice were randomly allocated to groups in all experiments. Two tailed paired and unpaired *t*-tests and ordinary one-way ANOVA were used when appropriate. Actual p values are presented for each data set. The criterion for statistical significance was $p < 0.05$. Boxplots presented in the figures depict mean; 25th; 75th percentile and SD.

Further information and requests for resources and reagents should be directed to and will be fulfilled by the Lead Contact, Alexander Binshtok (alexander.binshtok@mail.huji.ac.il).

Data and code availability

All datasets generated during and/or analyzed during the current study are available in the main text, the supplementary materials or upon request from the Lead Contact, Alexander Binshtok (alexander.binshtok@mail.huji.ac.il). Original/source data for Figures 6-7 in the paper will be available on the ModelDB repository.

References

Balasubramanyan, S., Stemkowski, P.L., Stebbing, M.J., and Smith, P.A. (2006). Sciatic chronic constriction injury produces cell-type-specific changes in the electrophysiological properties of rat substantia gelatinosa neurons. Journal of Neurophysiology *96*, 579–590.

Bardoni, R., Shen, K.F., Li, H., Jeffry, J., Barry, D.M., Comitato, A., Li, Y.Q., and Chen, Z.F. (2019). Pain Inhibits GRPR Neurons via GABAergic Signaling in the Spinal Cord. Scientific Reports *9*, 1–11.

Barkai, O., Goldstein, R.H., Caspi, Y., Katz, B., Lev, S., and Binshtok, A.M. (2017). The role of Kv7/M potassium channels in controlling ectopic firing in nociceptors. Frontiers in Molecular Neuroscience *10*.

Barkai, O., Puig, S., Lev, S., Title, B., Katz, B., Eli-Berchoer, L., Gutstein, H.B., and Binshtok, A.M. (2019). Platelet-derived growth factor activates nociceptive neurons by inhibiting M-current and contributes to inflammatory pain. Pain *160*, 1281–1296.

Barkai, O., Butterman, R., Katz, B., Lev, S., and Binshtok, A.M. (2020). The input-output relation of primary nociceptive neurons is determined by the morphology of the peripheral nociceptive terminals. J Neurosci *28*, 1520–1546.

Basbaum, A.I., Bautista, D.M., Scherrer, G.G., and Julius, D. (2009). Cellular and Molecular Mechanisms of Pain. Cell *139*, 267–284.

Binshtok, A.M., Wang, H., Zimmermann, K., Amaya, F., Vardeh, D., Shi, L., Brenner, G.J., Ji, R.R., Bean, B.P., Woolf, C.J., et al. (2008). Nociceptors are interleukin-1β sensors. Journal of Neuroscience *28*, 14062–14073.

Braz, J., Solorzano, C., Wang, X., and Basbaum, A.I. (2014). Transmitting Pain and Itch Messages: A Contemporary View of the Spinal Cord Circuits that Generate Gate Control. Neuron *82*, 522–536.

Bráz, J.M., Sharif-Naeini, R., Vogt, D., Kriegstein, A., Alvarez-Buylla, A., Rubenstein, J.L., and Basbaum, A.I. (2012). Forebrain GABAergic Neuron Precursors Integrate into Adult Spinal Cord and Reduce Injury-Induced Neuropathic Pain. Neuron *74*, 663–675.

Cho, K., Jang, J.H., Kim, S.P., Lee, S.H., Chung, S.C., Kim, I.Y., Jang, D.P., and Jung, S.J. (2016). Analysis of Nociceptive Information Encoded in the Temporal Discharge Patterns of Cutaneous C-Fibers. Front Comput Neurosci *10*.

Cirillo, G., De Luca, D., and Papa, M. (2012). Calcium imaging of living astrocytes in the mouse spinal cord following sensory stimulation. Neural Plasticity *2012*.

Coderre, T.J., and Melzack, R. (1985). Increased pain sensitivity following heat injury involves a central mechanism. Behavioural Brain Research *15*, 259–262.

Coull, J.A.M., Boudreau, D., Bachand, K., Prescott, S.A., Nault, F., Sík, A., de Koninck, P., and de Koninck, Y. (2003). Trans-synaptic shift in anion gradient in spinal lamina I neurons as a mechanism of neuropathic pain. Nature *424*, 938–942.

Coull, J.A.M., Beggs, S., Boudreau, D., Boivin, D., Tsuda, M., Inoue, K., Gravel, C., Salter, M.W., and de Koninck, Y. (2005). BDNF from microglia causes the shift in neuronal anion gradient underlying neuropathic pain. Nature *438*, 1017–1021.

Duan, B., Cheng, L., Bourane, S., Britz, O., Padilla, C., Garcia-Campmany, L., Krashes, M., Knowlton, W., Velasquez, T., Ren, X., et al. (2014). Identification of spinal circuits transmitting and gating mechanical pain. Cell *159*, 1417–1432.

Foster, E., Wildner, H., Tudeau, L., Haueter, S., Ralvenius, W.T., Jegen, M., Johannssen, H., Hösli, L., Haenraets, K., Ghanem, A., et al. (2015). Targeted ablation, silencing, and activation establish glycinergic dorsal horn neurons as key components of a spinal gate for pain and itch. Neuron *85*, 1289–1304.

François, A., Low, S.A., Sypek, E.I., Christensen, A.J., Sotoudeh, C., Beier, K.T., Ramakrishnan, C., Ritola, K.D., Sharif-Naeini, R., Deisseroth, K., et al. (2017). A Brainstem-Spinal Cord Inhibitory Circuit for Mechanical Pain Modulation by GABA and Enkephalins. Neuron *93*, 822-839.e6.

Goldstein, R.H., Barkai, O., Íñigo-Portugués, A., Katz, B., Lev, S., and Binshtok, A.M. (2019). Location and Plasticity of the Sodium Spike Initiation Zone in Nociceptive Terminals In Vivo. Neuron *102*, 801-812.e5.

Górski, T., Depannemaecker, D., and Destexhe, A. (2021). Conductance-based adaptive exponential integrate-and-fire model. Neural Computation *33*, 41–66.

Grudt, T.J., and Perl, E.R. (2002). Correlations between neuronal morphology and electro-physiological features in the rodent superficial dorsal horn. Journal of Physiology *540*, 189–207.

Gudes, S., Barkai, O., Caspi, Y., Katz, B., Lev, S., and Binshtok, A.M. (2015). The role of slow and persistent ttx-resistant sodium currents in acute tumor necrosis factor- α-mediated increase in nociceptors excitability. Journal of Neurophysiology *113*, 601–619.

Hachisuka, J., Koerber, H.R., and Ross, S.E. (2020). Selective-cold output through a distinct subset of lamina i spinoparabrachial neurons. Pain *161*, 185–194.

Harding, E.K., Fung, S.W., and Bonin, R.P. (2020). Insights Into Spinal Dorsal Horn Circuit Function and Dysfunction Using Optical Approaches. Frontiers in Neural Circuits *14*, 31.

Hentall, I. (1977). A novel class of unit in the substantia gelatinosa of the spinal cat. Experimental Neurology *57*, 792–806.

Hucho, T., and Levine, J.D. (2007). Signaling pathways in sensitization: toward a nociceptor cell biology. Neuron *55*, 365–376.

Hughes, D.I., Todd, A.J., and Hughes DavidIHughes, D.I. (2020). Central Nervous System Targets: Inhibitory Interneurons in the Spinal Cord Inhibitory Interneurons in the Spinal Dorsal Horn.

Johannssen, H.C., and Helmchen, F. (2010). In vivo Ca2+ imaging of dorsal horn neuronal populations in mouse spinal cord. Journal of Physiology *588*, 3397–3402.

Johannssen, H.C., and Helmchen, F. (2013). Two-photon imaging of spinal cord cellular networks. Experimental Neurology *242*, 18–26.

Julius, D., and Basbaum, A.I. (2001). Molecular mechanisms of nociception. Nature *413*, 203–210.

Kohama, I., Ishikawa, K., and Kocsis, J.D. (2000). Synaptic reorganization in the substantia gelatinosa after peripheral nerve neuroma formation: Aberrant innervation of lamina II neurons by Aβ afferents. Journal of Neuroscience *20*, 1538–1549.

Kohro, Y., Matsuda, T., Yoshihara, K., Kohno, K., Koga, K., Katsuragi, R., Oka, T., Tashima, R., Muneta, S., Yamane, T., et al. (2020). Spinal astrocytes in superficial laminae gate brainstem descending control of mechanosensory hypersensitivity. Nature Neuroscience *23*, 1376–1387.

Kumazawa, T., and Perl, E.R. (1978). Excitation of marginal and substantia gelatinosa neurons in the primate spinal cord: Indications of their place in dorsal horn functional organization. Journal of Comparative Neurology *177*, 417–434.

Kuner, R. (2010). Central mechanisms of pathological pain. Nature Medicine *16*, 1258–1266.

Lee, K.Y., Ratté, S., and Prescott, S.A. (2019). Excitatory neurons are more disinhibited than inhibitory neurons by chloride dysregulation in the spinal dorsal horn. ELife *8*.

Li, J., and Baccei, M.L. (2011). Pacemaker neurons within newborn spinal pain circuits. Journal of Neuroscience *31*, 9010–9022.

Li, Y.Q., Li, H., Yang, K., Kaneko, T., and Mizuno, N. (2000). Morphologic features and electrical membrane properties of projection neurons in the marginal layer of the medullary dorsal horn of the rat. Journal of Comparative Neurology *424*, 24–36.

Lu, Y., and Perl, E.R. (2003). A specific inhibitory pathway between substantia gelatinosa neurons receiving direct C-fiber input. Journal of Neuroscience *23*, 8752–8758.

Lu, Y., and Perl, E.R. (2005). Modular organization of excitatory circuits between neurons of the spinal superficial dorsal horn (laminae I and II). Journal of Neuroscience *25*, 3900–3907.

Lu, J., Li, C., Singh-Alvarado, J., Zhou, Z.C., Fröhlich, F., Mooney, R., and Wang, F. (2018). MIN1PIPE: A Miniscope 1-Photon-Based Calcium Imaging Signal Extraction Pipeline. Cell Reports *23*, 3673–3684.

Lucas-Romero, J., Rivera-Arconada, I., Roza, C., and Lopez-Garcia, J.A. (2018). Origin and classification of spontaneous discharges in mouse superficial dorsal horn neurons. In Scientific Reports, (Nature Publishing Group), pp. 1–11.

Matsumura, S., Taniguchi, W., Nishida, K., Nakatsuka, T., and Ito, S. (2015). In vivo two-photon imaging of structural dynamics in the spinal dorsal horn in an inflammatory pain model. European Journal of Neuroscience *41*, 987–995.

McCoy, E.S., Taylor-Blake, B., Street, S.E., Pribisko, A.L., Zheng, J., and Zylka, M.J. (2013). Peptidergic CGRPα Primary Sensory Neurons Encode Heat and Itch and Tonically Suppress Sensitivity to Cold. Neuron *78*, 138–151.

Moore, K.A., Kohno, T., Karchewski, L.A., Scholz, J., Baba, H., and Woolf, C.J. (2002). Partial peripheral nerve injury promotes a selective loss of GABAergic inhibition in the superficial dorsal horn of the spinal cord. Journal of Neuroscience *22*, 6724–6731.

Narikawa, K., Furue, H., Kumamoto, E., and Yoshimura, M. (2000). In Vivo Patch-Clamp Analysis of IPSCs Evoked in Rat Substantia Gelatinosa Neurons by Cutaneous Mechanical Stimulation. Journal of Neurophysiology *84*, 2171–2174.

Netser, S., Haskal, S., Magalnik, H., Bizer, A., and Wagner, S. (2019). A system for tracking the dynamics of social preference behavior in small rodents. Journal of Visualized Experiments *2019*, e60336.

Nimmerjahn, A., Kirchhoff, F., Kerr, J.N.D., and Helmchen, F. (2004). Sulforhodamine 101 as a specific marker of astroglia in the neocortex in vivo. Nature Methods *1*, 31–37.

Ossipov, M.H., Dussor, G.O., and Porreca, F. (2010). Central modulation of pain. Journal of Clinical Investigation *120*, 3779–3787.

Paricio-Montesinos, R., Schwaller, F., Udhayachandran, A., Rau, F., Walcher, J., Evangelista, R., Vriens, J., Voets, T., Poulet, J.F.A., and Lewin, G.R. (2020). The Sensory Coding of Warm Perception. Neuron *106*, 830-841.e3.

Peirs, C., Dallel, R., and Todd, A.J. (2020). Recent advances in our understanding of the organization of dorsal horn neuron populations and their contribution to cutaneous mechanical allodynia. Journal of Neural Transmission *127*, 505–525.

Polgár, E., Durrieux, C., Hughes, D.I., and Todd, A.J. (2013). A Quantitative Study of Inhibitory Interneurons in Laminae I-III of the Mouse Spinal Dorsal Horn. PLoS ONE *8*, 78309.

Prescott, S.A., and de Koninck, Y. (2002). Four cell types with distinctive membrane properties and morphologies in lamina I of the spinal dorsal horn of the adult rat. Journal of Physiology *539*, 817–836.

Prescott, S.A., and De Koninck, Y. (2002). Four cell types with distinctive membrane properties and morphologies in lamina I of the spinal dorsal horn of the adult rat. Journal of Physiology *539*, 817–836.

Prescott, S.A., and Ratté, S. (2012). Pain processing by spinal microcircuits: Afferent combinatorics. Current Opinion in Neurobiology *22*, 631–639.

Punnakkal, P., von Schoultz, C., Haenraets, K., Wildner, H., and Zeilhofer, H.U. (2014). Morphological, biophysical and synaptic properties of glutamatergic neurons of the mouse spinal dorsal horn. Journal of Physiology *592*, 759–776.

Ran, C., and Chen, X. (2019). Probing the coding logic of thermosensation using spinal cord calcium imaging. Experimental Neurology *318*, 42–49.

Ran, C., Hoon, M.A., and Chen, X. (2016). The coding of cutaneous temperature in the spinal cord. Nature Neuroscience *19*, 1201–1209.

Roza, C., Mazo, I., Rivera-Arconada, I., Cisneros, E., Alayón, I., and López-García, J.A. (2016). Analysis of spontaneous activity of superficial dorsal horn neurons in vitro: neuropathy-induced changes. Pflugers Archiv European Journal of Physiology *468*, 2017–2030.

Ruscheweyh, R., Ikeda, H., Heinke, B., and Sandkühler, J. (2004). Distinctive membrane and discharge properties of rat spinal lamina I projection neurones in vitro. Journal of Physiology *555*, 527–543.

Sandkühler, J., and Eblen-Zajjur, A.A. (1994). Identification and characterization of rhythmic nociceptive and non-nociceptive spinal dorsal horn neurons in the rat. Neuroscience *61*, 991–1006.

Schoffnegger, D., Heinke, B., Sommer, C., and Sandkühler, J. (2006). Physiological properties of spinal lamina II GABAergic neurons in mice following peripheral nerve injury. Journal of Physiology *577*, 869–878.

Shields, S.D., Cheng, X., Üçeyler, N., Sommer, C., Dib-Hajj, S.D., and Waxman, S.G. (2012). Sodium channel NA v1.7 is essential for lowering heat pain threshold after burn injury. Journal of Neuroscience *32*, 10819–10832.

Takazawa, T., and MacDermott, A.B. (2010). Glycinergic and GABAergic tonic inhibition fine tune inhibitory control in regionally distinct subpopulations of dorsal horn neurons. Journal of Physiology *588*, 2571–2587.

Takiguchi, N., Yoshida, M., Taniguchi, W., Hashizume, H., Yamada, H., Miyazaki, N., Nishio, N., and Nakatsuka, T. (2012). Distinct Degree of Radiculopathy at Different Levels of Peripheral Nerve Injury. Molecular Pain *8*, 1744-8069-8–31.

Todd, A.J. (2010). Neuronal circuitry for pain processing in the dorsal horn. Nature Reviews Neuroscience *11*, 823–836.

Uta, D., Kato, G., Doi, A., Andoh, T., Kume, T., Yoshimura, M., and Koga, K. (2019). Animal models of chronic pain increase spontaneous glutamatergic transmission in adult rat spinal dorsal horn in vitro and in vivo. Biochemical and Biophysical Research Communications *512*, 352–359.

Wang, F., Bé, E., C^ Oté, S.L., Desrosiers, P., Prescott, S.A., C^ Oté, D.C., De, Y., and Correspondence, K. (2018). Sensory Afferents Use Different Coding Strategies for Heat and Cold. CellReports *23*, 2001–2013.

Wang, X., Zhang, J., Eberhart, D., Urban, R., Meda, K., Solorzano, C., Yamanaka, H., Rice, D., and Basbaum, A.I. (2013). Excitatory superficial dorsal horn interneurons are functionally heterogeneous and required for the full behavioral expression of Pain and Itch. Neuron *78*, 312–324.

Waxman, S.G., and Zamponi, G.W. (2014). Regulating excitability of peripheral afferents: emerging ion channel targets. Nat Neurosci *17*, 153–163.

Yamanaka, M., Taniguchi, W., Nishio, N., Hashizume, H., Yamada, H., Yoshida, M., and Nakatsuka, T. (2015). In vivo patch-clamp analysis of the antinociceptive actions of TRPA1 activation in the spinal dorsal horn. Molecular Pain *11*.

Yarmolinsky, D.A., Peng, Y., Pogorzala, L.A., Rutlin, M., Hoon, M.A., and Zuker, C.S. (2016). Coding and Plasticity in the Mammalian Thermosensory System. Neuron *92*, 1079–1092.

Zhang, H., Li, Y., Yang, Q., Liu, X.G., and Dougherty, P.M. (2018). Morphological and physiological plasticity of spinal lamina II GABA neurons is induced by sciatic nerve chronic constriction injury in mice. Frontiers in Cellular Neuroscience *12*.